JGR Oceans

RESEARCH ARTICLE
10.1029/2024JC021343

Strengthening of the Equatorial Pacific Upper-Ocean Circulation Over the Past Three Decades

Franz Philip Tuchen[1,2], Renellys C. Perez[2], Gregory R. Foltz[2], Michael J. McPhaden[3], and Rick Lumpkin[2]

[1]Cooperative Institute for Marine and Atmospheric Studies, Rosenstiel School of Marine, Atmospheric, and Earth Science, University of Miami, Miami, FL, USA, [2]NOAA Atlantic Oceanographic and Meteorological Laboratory, Miami, FL, USA, [3]NOAA Pacific Marine Environmental Laboratory, Seattle, WA, USA

Key Points:

- 30 years of observations show a wind-driven strengthening of equatorial Pacific surface zonal currents by ∼20% and poleward flow by ∼20%−60%
- The subsurface Equatorial Undercurrent intensified above its core depth, primarily in the central to eastern Pacific
- Long-term moored observations of subsurface velocity and temperature show a significant basin-wide steepening of the equatorial thermocline

Supporting Information:

Supporting Information may be found in the online version of this article.

Correspondence to:

F. P. Tuchen,
franz.philip.tuchen@noaa.gov;
fpt10@miami.edu

Citation:

Tuchen, F. P., Perez, R. C., Foltz, G. R., McPhaden, M. J., & Lumpkin, R. (2024). Strengthening of the equatorial Pacific upper-ocean circulation over the past three decades. *Journal of Geophysical Research: Oceans*, *129*, e2024JC021343. https://doi.org/10.1029/2024JC021343

Received 14 MAY 2024
Accepted 26 SEP 2024

Author Contributions:

Conceptualization: Franz Philip Tuchen
Data curation: Rick Lumpkin
Formal analysis: Franz Philip Tuchen
Funding acquisition: Renellys C. Perez, Gregory R. Foltz
Investigation: Franz Philip Tuchen
Methodology: Franz Philip Tuchen, Renellys C. Perez, Gregory R. Foltz, Michael J. McPhaden
Software: Franz Philip Tuchen
Supervision: Renellys C. Perez, Gregory R. Foltz
Visualization: Franz Philip Tuchen
Writing – original draft: Franz Philip Tuchen

Abstract Thirty years (1993–2022) of concurrent satellite and in-situ observations show a long-term strengthening of the equatorial Pacific upper-ocean circulation. Enhanced southeasterly and cross-equatorial winds have caused an annual mean, basin-wide acceleration of the equatorial westward near-surface currents by ∼20% and an acceleration of poleward flow north (south) of the equator by ∼60% (∼20%). Additional moored velocity data reveal a deepening of the Equatorial Undercurrent (EUC) core at 170°W and significant shoaling at 140°W and 110°W, but no significant changes in EUC core velocity. The strongest subsurface zonal velocity trends are observed above the EUC core in the central to eastern Pacific and occur before and after the seasonal maximum of EUC core velocity, causing enhanced upper-ocean vertical current shear. Consistent with trends of the 20°C isotherm depth along the equatorial Pacific, a significant basin-wide steepening of the equatorial thermocline is observed. Both the accelerating equatorial current system and the enhanced thermocline slope are consistent with an observed steepening of the zonal sea surface height gradient due to increased wind-driven westward mass transport at the surface. During February-March, both surface and subsurface currents along the equator show eastward velocity trends, in contrast to westward near-surface current trends during the remainder of the year. The trend reversal is attributed to both a long-term shift in equatorial Kelvin wave activity and to the impact of strong interannual variability due to El Niño Southern Oscillation and other modes of natural variability on decadal to multidecadal time scales.

Plain Language Summary Thirty years (1993–2022) of temporally overlapping satellite and in-situ observations reveal a long-term strengthening of the equatorial Pacific circulation in the upper 200 m. Both the west-east (zonal) and south-north (meridional) surface atmospheric winds typically observed in the tropical Pacific intensified. As a result, westward near-surface currents in the central equatorial Pacific accelerated by ∼20%, while poleward currents accelerated by ∼60% (∼20%) north (south) of the equator. The strongest trends in zonal velocity are observed above the core of the Equatorial Undercurrent. While the subsurface current in the central and eastern Pacific shoaled by 12 m, it deepened in the western Pacific by 6 m, which aligns with trends of the 20°C isotherm depth. Both the accelerating equatorial currents and the steeper thermocline slope are consistent with a steepening west-east slope of sea surface height due to increased westward water mass transport. Our results show that a shift in equatorial wave activity and strong interannual variability cause eastward velocity anomalies in the observed surface and subsurface current trends during February-March. Between 1993 and 2022, long-term equatorial circulation trends persist, but these trends are modified by natural events at both interannual timescales such as El Niño and La Niña events, and longer timescales.

1. Introduction

Climate variability in the tropical Pacific Ocean plays a crucial role in the global climate system and significantly influences fluctuations in global surface air temperature (Capotondi et al., 2023; McPhaden et al., 2006). While global mean sea surface temperature (SST) and upper-ocean heat content continue to rise due to increasing external radiative forcing (Cheng et al., 2024; von Schuckmann et al., 2020; Trenberth et al., 2014), parts of the tropical South Pacific (180°W−80°W, 20°S−0°S) have experienced a remarkable cooling trend of more than −0.5°C over the past 3 decades (Figure 1; see also Latif et al., 2023), resembling a La Niña-like cooling pattern (Kosaka & Xie, 2013) which most state-of-the-art climate models fail to represent accurately (An et al., 2012; Fu et al., 2024; Latif et al., 2023). Previous studies have identified the tropical South Pacific cooling as one of the main drivers of the global warming hiatus observed at the beginning of the 21st century (Kosaka & Xie, 2013).

Writing – review & editing: Franz Philip Tuchen, Renellys C. Perez, Gregory R. Foltz, Michael J. McPhaden, Rick Lumpkin

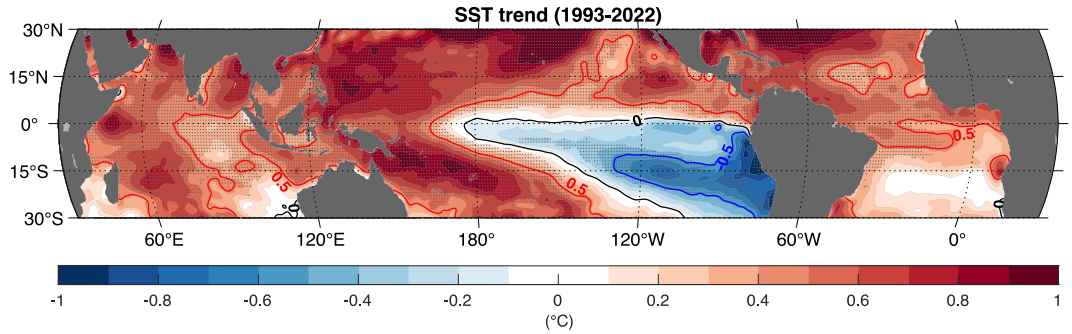

Figure 1. Satellite-based SST trend between 1993 and 2022 from OI-SST (version 2.1). Red color shading indicates a positive warming trend. Blue color shading indicates cooling. Speckled regions indicate significant SST trends at 95% confidence.

However, the contributions to tropical South Pacific cooling from external forcing and modes of internal variability such as the Interdecadal Pacific Oscillation (IPO) (Latif et al., 1997; Power et al., 1999, 2021), Pacific Decadal Oscillation (PDO) (Mantua et al., 1997; Zhang et al., 1997), and North Pacific Gyre Oscillation (NPGO) (Bond et al., 2003; Capotondi & Qiu, 2023; Di Lorenzo et al., 2008) are still under debate (Heede & Fedorov, 2023).

Both the IPO and PDO are dominated by variations on time scales longer than 10 years. The IPO is defined as the difference between SST anomalies averaged over the equatorial Pacific and the average of SST anomalies over the northwestern and southwestern Pacific (Henley et al., 2015). In its positive phase, the IPO is characterized by an anomalously warm tropical Pacific and anomalously cold northern and southern Pacific, while tropical Pacific SST is below normal in its negative phase (Power et al., 1999). The PDO is defined as the leading principal component of North Pacific (poleward of 20°N) monthly SST variability (Mantua et al., 1997). The tropical Pacific SST signature of the PDO is similar to that of the IPO (Newman et al., 2016), as both modes are associated with cool (warm) anomalies in the tropical Pacific during their negative (positive) phase. The IPO and PDO are strongly affected by El Niño Southern Oscillation (ENSO)-induced variability at interannual timescales, by circulation changes at longer timescales (Capotondi et al., 2023), and by stochastic atmospheric forcing (Newman et al., 2016). Both the IPO and PDO have mostly been in a negative phase since the beginning of the 21st century (England et al., 2014; Newman et al., 2016). Using climate model simulations, Meehl et al. (2013) argue that tropical cooling during negative phases of the IPO can offset externally forced warming of the tropics, leading to an overall warming hiatus period. Recently, the tropical South Pacific cooling over the past three decades has been attributed to the ongoing negative phase of the PDO, which is associated with increased latent heat loss by the ocean due to an acceleration of the tropical Pacific atmospheric circulation (Latif et al., 2023).

Analysis of model output and reanalysis data suggests that wind-driven changes in tropical ocean dynamics, such as enhanced shallow overturning cells and equatorial upwelling, also contributed to cooling near the equator (England et al., 2014). The shallow overturning cells are comprised of two partially overlapping overturning cells: (a) the tropical cells confined to 2–5° off the equator (Perez et al., 2010) and (b) the subtropical cells which are typically estimated at 9°–10° off the equator (McPhaden & Zhang, 2002; Schott et al., 2004). England et al. (2014) examined tropical Pacific SST trends and concluded that much of the global warming hiatus observed during 1992–2011 was due to intensified trade winds over the tropical Pacific that led to accelerated poleward surface divergence, off-equatorial downwelling, equatorward convergence in the thermocline, and equatorial upwelling (i.e., an intensification of the shallow overturning cells). However, since the end of the global warming hiatus period in 2013, global SST has resumed its long-term increase, despite the apparent ongoing acceleration of tropical Pacific winds (Heede & Fedorov, 2023; Latif et al., 2023). Possibly, increasing external forcing (Storto & Yang, 2024) has begun to exceed the cooling effect that the tropical South Pacific exerts on global SST, or natural variability outside of the tropical Pacific is causing stronger warming which offsets the Pacific cooling effect. After the 2015/16 El Niño, global mean surface temperature anomalies plateaued again for several years until 2023, though at a higher level (0.9°C–1.0°C, with respect to 1951–1980) than during the global warming hiatus (0.6°C–0.7°C, with respect to 1951–1980) at the beginning of the 21st century (GISTEMP Team, 2024; Lenssen et al., 2019).

Large-scale and long-term changes in SST due to natural modes of variability like the IPO and PDO drive changes in atmospheric winds and ocean currents, with potential feedbacks between these variables (M. Wang et al., 2024). However, the role of ocean currents in the large-scale redistribution of heat in the tropical Pacific, and their long-term variability and trends, have been less studied due to sparse surface and subsurface observations both in space and time. Strong, large-scale ocean currents in the tropics drive horizontal temperature advection, equatorial upwelling, and vertical and horizontal current shear leading to shear-driven mixing in regions of strong currents. An improved understanding of decadal changes in ocean currents will lead to an improved understanding of the role of ocean dynamics in SST and ocean heat content variability on long time scales.

While satellite observations have provided valuable long-term records of SST and sea surface height (SSH) necessary to assess decadal climate variability and trends, observing and understanding changes in tropical ocean dynamics have been challenging due to the scarcity of in-situ current velocity observations and challenges of inferring surface velocities from satellite altimetry near the equator. Long-term records of subsurface currents are only available at a subset of the equatorial moored surface buoys from the Tropical Atmosphere Ocean (TAO) array (McPhaden et al., 2010, 2023). Using parts of these data, Amaya et al. (2015) showed that the core of the Pacific Equatorial Undercurrent (EUC) at the mooring sites accelerated on average by about 7 cm s^{-1} $decade^{-1}$ between 1990 and 2009. However, obtaining direct observations of changes to the large-scale spatial patterns of surface and subsurface currents in the tropics has remained elusive. In addition, short time series are strongly influenced by interannual variability due to ENSO. For instance, Meinen et al. (2001) estimated vertical velocities in the equatorial Pacific from temperature and wind data between 1993 and 1999, but that time period was too short to infer long-term upwelling trends as the record was strongly impacted by the 1997/98 El Niño event. Hence, analyses of longer time series are needed to assess long-term variability and trends with more confidence. Recently, Hu et al. (2020) used a set of six different reanalysis products to show that the global mean circulation's kinetic energy increased between the early 1990s to early 2010s. In particular, the tropical oceans showed a pronounced increase in kinetic energy, which was partly attributed to natural variability associated with the negative PDO phase during that time period. However, model projections suggest that the global acceleration of upper ocean currents will continue beyond the time scale of natural decadal variability due to increased vertical stratification associated with anthropogenic warming, indicating a positive current response to external forcing (Peng et al., 2022).

In this study, we examine 30 year (1993–2022) trends of the equatorial Pacific upper-ocean circulation using a synthesis product of drifter observations, reanalysis winds, and satellite altimetry (Lumpkin & Garzoli, 2011) as well as moored velocity and temperature observations along the equator from the TAO array. The synthesis product allows for a detailed examination of trends in near-surface tropical currents, as well as their spatial coherence and variability across time scales. Such analysis has previously been limited to studies using model output or reanalysis products. Consequently, this study aims to serve as an important benchmark to validate model simulations and reanalysis products used to study tropical Pacific SST trends. By examining the observed spatial and temporal patterns of long-term trends in upper-ocean currents over the past three decades, we provide observational evidence for a significant wind-driven acceleration of equatorial Pacific near-surface and subsurface currents and examine the seasonal dependence of those trends. These circulation changes have occurred with and partially in response to a substantial steepening of the equatorial Pacific thermocline. Potential impacts of a steeper thermocline for ENSO variability will also be discussed.

2. Materials and Methods

2.1. Satellite and Reanalysis Data

Wind stress is derived from the ECMWF ERA5 horizontal wind speeds at 10 m provided on a 0.25° horizontal grid and at 1 hr intervals from January 1940 to present (Hersbach et al., 2020). The horizontal wind speed vector $\vec{u_{10}}$ is converted to horizontal wind stress $\vec{\tau}$ via a bulk formula:

$$\vec{\tau} = \rho_a \, c_D \, \vec{u_{10}} \, |\vec{u_{10}}|$$

where ρ_a is the density of air (1.22 kg m^{-3}), and c_D a dimensionless drag coefficient (0.0013) that has been used in previous studies of tropical ocean circulation (e.g., Kopte et al., 2018; Tuchen et al., 2019, 2020). Monthly

precipitation data are provided by the Global Precipitation Climatology Project (GPCP version 3.2) on a 0.5° horizontal grid from January 1983 to present (Huffman et al., 2022). Daily SSH data (version vDT2021) are provided by the Copernicus Marine Environment Monitoring Service from January 1993 to June 2023 at 0.25° horizontal resolution (Copernicus, 2023). Daily SST data from the NOAA Optimally Interpolated SST data set (OI-SST version 2.1) are available from September 1981 to present at 0.25° horizontal resolution (Huang et al., 2021).

2.2. Current Velocity Data

Global, daily maps of near-surface current velocities are provided by a synthesis of surface drifter velocities, Ekman velocities from reanalysis winds, and geostrophic velocities from satellite altimetry (Lumpkin & Garzoli, 2011; Perez et al., 2019; Tuchen, Perez, et al., 2022, 2024). The dataset, covering the time period from 1993 to 2022, is available on a 0.25° horizontal grid. Though this synthesis product underestimates high-frequency velocity fluctuations near the equator (Tuchen, Perez, et al., 2022, 2024), it remains a powerful tool for studying slowly varying changes in the zonal and meridional background flow in the tropics as shown by comparisons with buoy observations and reanalysis products (Tuchen, Perez, et al., 2022). In addition, we analyze in-situ observations of upper-ocean currents by Acoustic Doppler Current Profilers (ADCP) installed at a subset of the equatorial moored surface buoys of the TAO array. These observations are part of the Global Tropical Moored Buoy Array (GTMBA; McPhaden et al., 2010, 2023). Daily mean ADCP velocity data are available at 10 m vertical resolution from three sites: 0°, 170°W between May 1988 and January 2020 at depths between 20 and 250 m; 0°, 140°W between May 1990 and March 2022 at depths between 20 and 200 m; and 0°, 110°W between May 1991 and July 2020 at depths between 20 and 200 m. In addition, TAO moorings provide the long-term subsurface temperature measurements which are used to estimate the depth of the 20°C isotherm at a total of nine equatorial mooring sites (156°E, 165°E, 180°, 170°W, 155°W, 140°W, 125°W, 110°W, 95°W). The 20°C isotherm depth is a well-known proxy for the depth of the thermocline in the tropics.

2.3. Data Preparation, and Trend Calculation and Significance

In a first step, the individual daily time series are averaged into monthly mean time series. This helps to reduce computational costs and acts as a simple low-pass filter. To ensure consistency, all time series are limited to the 30 year time period of 1993–2022, even though some individual time series extend beyond this period. ADCP data at 0°, 170°W have one 3 year data gap from July 2006 to June 2009. ADCP data at 0°, 140°W have three 7–13 months data gaps: from September 1995 to September 1996, March 2014 to September 2014, and from April 2016 to January 2017. ADCP data at 0°, 110°W, exhibit two 1–2 years data gaps: from November 2006 to December 2008, and from July 2010 to August 2011. To facilitate linear trend calculations, these gaps were filled with climatological values. All linear trends and 95% confidence intervals are calculated using linear regression analysis of the monthly mean time series at each grid point (following the method described in Brandt et al., 2021). The linear trends presented in the analysis have been converted to decadal trend values (e.g., unit/decade). Uncertainty ranges of linear trend estimates are derived from the same 95% confidence intervals.

3. Global Tropical Wind, Precipitation and Sea Surface Height Trends

Tropical Pacific winds are characterized by the seasonal variation and meridional migration of the southeasterly trade winds (Figures 2b and 2d). The decadal trends in global tropical wind stress during 1993–2022 indicate a significant intensification of the southeasterly trade winds in the tropical Pacific (Figure 2a). The most notable increases in tropical Pacific zonal wind stress occur between 10°S and 2°N and between 170°E and 100°W (Figures 2a–2c), while the strongest increases in meridional wind stress are observed between 1°N and 6°N and 6°S and 1°N (Figures 2a–2d and 2e). Enhanced cross-equatorial (northward) wind stress has been found to modulate ENSO variability (Hu & Fedorov, 2018). There is also a weakening of the northeasterly trade winds north of 10°N (Figure 2a). Trends in wind stress exhibit a pronounced seasonal dependence, with the highest increases in zonal wind stress occurring from March to May and in July and September, while meridional wind stress trends peak from May to December north of the equator. Our results further indicate increased cross-equatorial wind stress that leads to increased convergence of air north of the equator along the mean location of the Pacific Intertropical Convergence Zone (ITCZ; 170°E−100°W, 5°N−10°N; Figures 3a and 3b). As a consequence, precipitation within the Pacific ITCZ has increased by 9% (Figures 2a and 3e–3f), while precipitation in the tropical South Pacific has decreased by 35% (Figures 2a and 3e, 3h), consistent with the pattern of

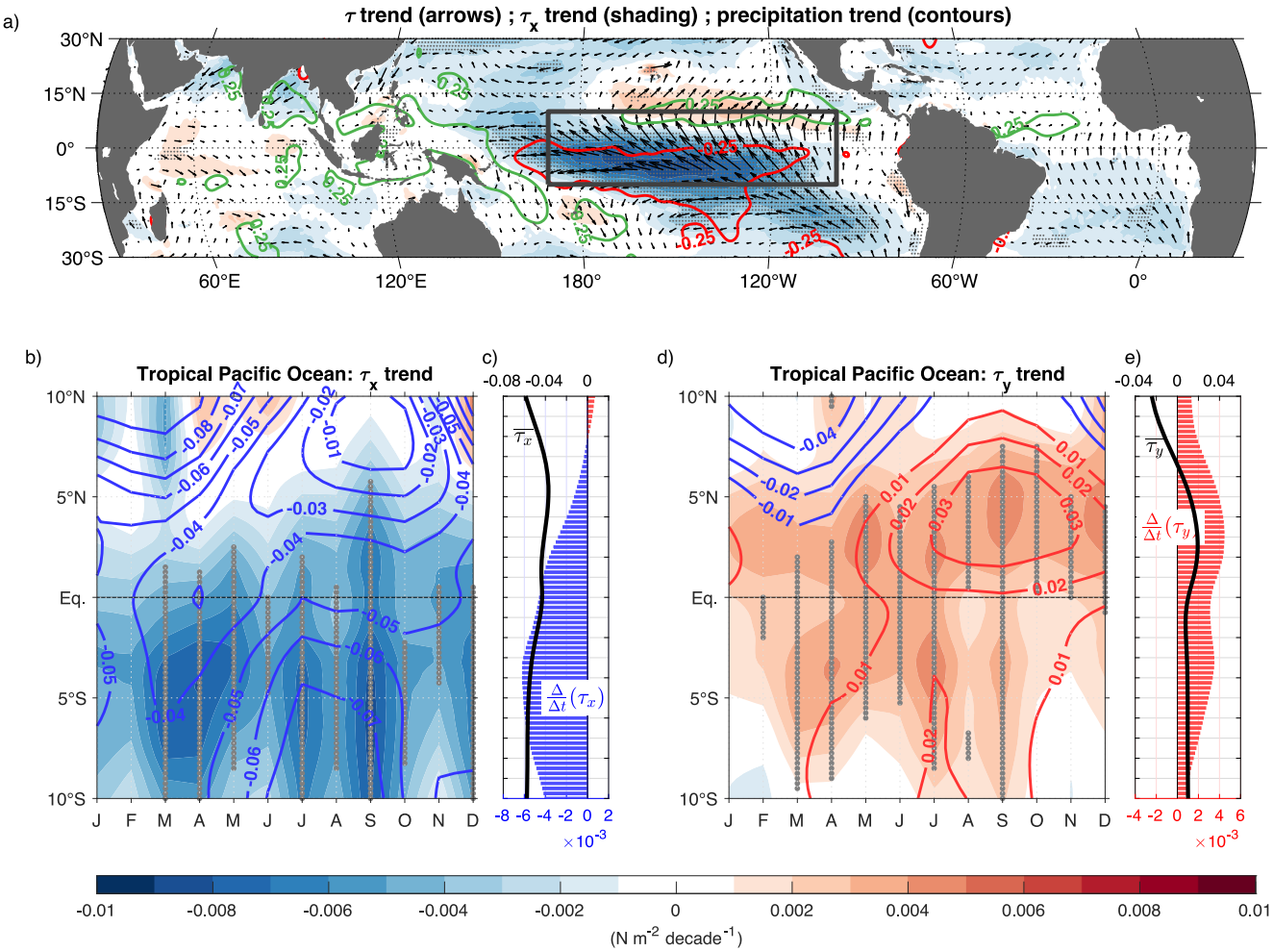

Figure 2. (a) Decadal trends of zonal wind stress (τ_x, color shading) and horizontal wind stress ($\boldsymbol{\tau}$, arrows) and precipitation (color contours) in the tropics between 1993 and 2022. The ±0.25 mm day^{-1} decade^{-1} contour lines are indicated with negative trends in red and positive trends in green. Speckled regions indicate significant τ_x trends at 95% confidence. (b) Decadal trend of τ_x (color shading) and climatological τ_x (color contours) as a function of month and zonally averaged for the central tropical Pacific Ocean region (170°E–100°W) indicated in (a). Blue contour lines indicate negative climatological τ_x and red contour lines indicate positive climatological τ_x (in N m^{-2}). (c) Zonally averaged (170°E–100°W) annual mean τ_x (black line; N m^{-2}) and annual mean decadal trend (red and blue bars; N m^{-2} decade^{-1}). (d) Same as (b) but for meridional wind stress, τ_y. (e) Same as (c) but for meridional wind stress, τ_y. Gray dots in (b) and (d) indicate significant trends at 95% confidence. The same color bar is used for the panels (a), (b), and (d).

tropical Pacific precipitation trends shown by Adler et al. (2017). Precipitation has also increased near the Maritime Continent, consistent with the increase in western Pacific trade winds and surface convergence (Figures 2a and 3a, 3e). The spatial distribution of precipitation trends in the tropical Pacific and over the Maritime Continent is also in general agreement with SST trends (Figure 1) in these regions: increased precipitation over warming waters and reduced precipitation over cooling waters. However, reduced precipitation is also observed west of the westernmost extent of the SST cooling pattern (Figure 1; black contour line), between 180° and 175°W, where increased horizontal divergence of wind stress appears to be the main cause of reduction, possibly connected to a southwestward shift of the South Pacific Convergence Zone (Figure 3a). In general, increased wind stress convergence corresponds to more precipitation due to increased convection mainly in the tropics. However, this relation does not seem to hold in the region just south of the equator where we observe increased wind stress convergence and reduced rainfall, or in the southeastern Pacific Ocean where mean rainfall is close to zero and no rainfall response is expected due to changes in wind stress convergence. In these regions, it is likely that other factors are important and more complex dynamics are probably at play. The reduction in precipitation in the tropical South Pacific is particularly remarkable from a global tropical perspective as neither the Indian nor the Atlantic Ocean has experienced comparable trends in precipitation.

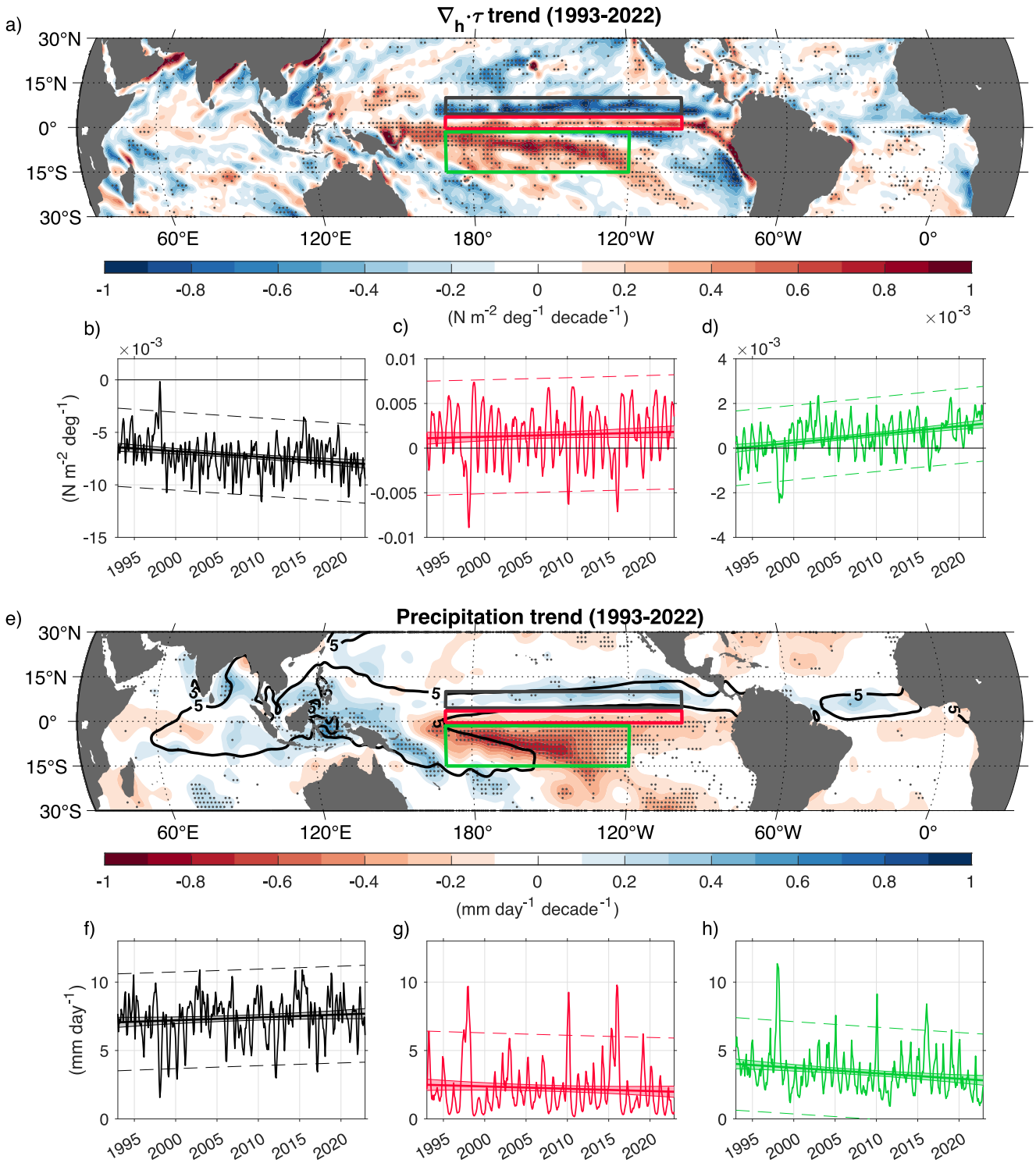

Figure 3. (a) Decadal trend of horizontal wind stress divergence ($\nabla_h \cdot \boldsymbol{\tau}$) in the tropics. Three regions are indicated, in the tropical North Pacific (170°E−100°W, 5°N−10°N; black box), equatorial Pacific (170°E−100°W, 2°S−5°N; red box), and in the tropical South Pacific (170°E−120°W, 15°S−2°S; green box). Speckled regions indicate significant $\nabla_h \cdot \boldsymbol{\tau}$ trends at 95% confidence. Monthly time series of $\nabla_h \cdot \boldsymbol{\tau}$ averaged in the (b) tropical North Pacific, (c) equatorial Pacific, and (d) tropical South Pacific. (e) Decadal trend of precipitation in the tropics. Note the color map is flipped for this panel. The black contour in (e) represents the climatological 5 mm day^{-1} isoline. Speckled regions indicate significant precipitation trends at 95% confidence. The same three regions as in (a) are depicted. Monthly time series of precipitation averaged in the (f) tropical North Pacific, (g) equatorial Pacific, and (h) tropical South Pacific. In (b)–(d) and (f)–(h), the linear trends (thick lines), 95% confidence interval (thin solid lines), and the 95% prediction interval (dashed lines) are indicated.

Winds in the tropical Pacific have unique trends with magnitudes that are not observed in the Indian or Atlantic Ocean (Figure 2a). In the western equatorial Indian Ocean, both zonal and meridional wind stress display elevated trends that weaken the seasonal cycle of wind stress in this region, though the trends are not nearly as strong as those in the Pacific (Figures S1a-b in Supporting Information S1). Normally, the Indian Ocean experiences a pronounced seasonal cycle with maximum wind stress during boreal summer during the Southwest Monsoon and upwelling off the coast of Somalia (Schott & McCreary, 2001). However, the observed reduction of the seasonal cycle suggests a weakening of both features (Figures S1a-b in Supporting Information S1). Increased easterlies in the tropical Pacific have been shown to contribute to a general strengthening of the zonal atmospheric circulation in the tropics, that is, the Walker Circulation (Heede & Fedorov, 2023). As a consequence, enhanced convection over the Maritime Continent is likely related to both enhanced subsidence and westerly wind trends in the western Indian Ocean.

In the southeastern Atlantic Ocean, wind stress is generally southeasterly, that is, parallel to the coastline. This wind pattern causes seasonal coastal upwelling off Angola and Namibia, particularly in late boreal summer (e.g., Brandt et al., 2023). Wind stress trends in this region reveal strengthening of the zonal and meridional components (Figure 2a), especially during the upwelling season (Figures S1c-d in Supporting Information S1). Servain et al. (2014) document a similar strengthening of the Atlantic trade winds from different data sets over the period 1964–2012. These findings suggest a possible intensification of the seasonal upwelling in the southeastern Atlantic Ocean. The observed wind stress trends in the Atlantic Ocean are consistent with stronger warming in the North Atlantic Ocean compared to the South Atlantic (Latif et al., 2023), which causes an anomalous meridional pressure gradient that leads to southerly wind stress trends (Figure 2a).

Intensifying Pacific trade winds are increasing the transfer of momentum from the atmosphere to the upper ocean, enhancing the westward transport of water masses in the tropics and affecting the large-scale pattern of sea surface height (SSH). Between 1993 and 2022, SSH in the global tropics (30°S−30°N) rose by approximately 0.03 m decade^{-1} (Figure 4a). However, sea level rise in the western and eastern tropical Pacific is zonally asymmetric: SSH trends in the western tropical Pacific are about twice as large as the global tropical mean sea level rise, while SSH trends in the eastern Pacific are close to zero. This strong zonal asymmetry can be seen clearly when the global tropical annual mean SSH trend is removed (Figure 4b; see also Timmermann et al., 2010). When subtracting SSH averaged in the eastern equatorial Pacific (170°W−85°W, 3°S−3°N) from SSH averaged in the western equatorial Pacific (150°E−170°W, 3°S−3°N), a significant trend in the zonal SSH difference is found (Figure 4c). The time series also shows two pronounced dips in the zonal SSH difference during the strong 1997/98 and 2015/16 El Niño events. In 1997/98, the sign of the zonal SSH gradient even reversed, indicating a reversal of the zonal surface currents along the equator. The steepening trend in the zonal SSH gradient is particularly prominent from September to January (not shown). From a dynamical standpoint, a steeper SSH slope along the equatorial Pacific can be expected to induce a response in the equatorial zonal current system, which will be examined in the upcoming section.

4. Tropical Pacific Near-Surface and Subsurface Current Trends

In a next step, we analyze the response of the upper-ocean circulation in the equatorial Pacific to increased zonal and meridional wind stress. To gain a comprehensive understanding, we will use (a) the drifter-wind-altimetry synthesis, which provides a spatial and near-surface perspective, and (b) moored velocity data at three equatorial sites (170°W, 140°W, and 110°W) which allows for a discrete and subsurface perspective.

The tropical Pacific Ocean clearly has the most pronounced near-surface velocity trends (Figure 5a), although trends are also observed in the tropical Atlantic and Indian Ocean. In the equatorial Pacific, the major westward near-surface currents are the northern South Equatorial Current (nSEC) between 1°S and 2°N and the central South Equatorial Current (cSEC) between 6°S and 2°S, while the North Equatorial Countercurrent (NECC) flows eastward between 5°N and 8°N (Figure 5b). All three current bands have experienced a long-term acceleration from 1993 to 2022 (Figures 5a–5c). In particular, the equatorial Pacific (170°E−100°W, 2°S−2°N) near-surface westward flow, primarily associated with the nSEC, has increased by 19% ± 15% (Figures 5a–5c and 5f). Mean meridional velocity near the equator is dominated by Ekman divergence, which comprises northward velocities north of the equator and southward velocities south of the equator (contours in Figure 5d and black line in Figure 5e). We find a significant amplification of this flow pattern (color shading in Figure 5d) that is strongest north of the equator (Figures 5d–5e, 5g). With the trend toward more southerly winds near the equator (Figure 2e),

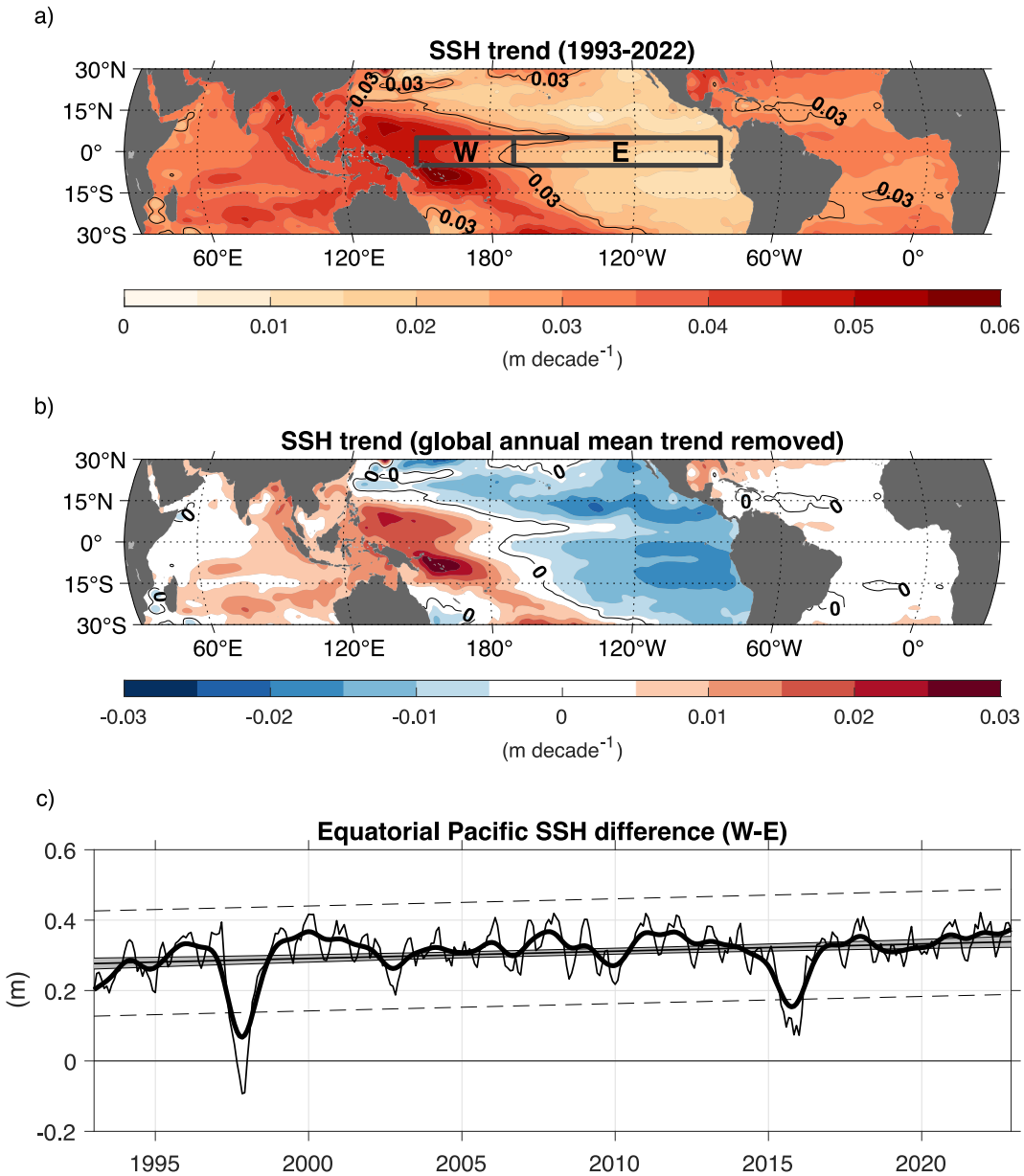

Figure 4. (a) Decadal trend of SSH in the tropics. The black isoline indicates the global tropical (30°S−30°N) annual mean SSH trend (0.03 m decade^{-1}). At 99.3% of all grid points, SSH trends are significant at 95% confidence. (b) Same as (a) but with the global tropical annual mean SSH trend removed. (c) Monthly SSH difference between the western (W; 150°E−170° W, 3°S−3°N) and eastern (E; 170°W−85°W, 3°S−3°N) equatorial Pacific regions indicated in (a). The thin curve represents the monthly time series, while the thick curve shows a 25 month running mean. The linear trend (thick solid line), 95% confidence interval (thin solid lines and gray shading), and the 95% prediction interval (dashed lines) are indicated.

an upwind shift of the center of meridional velocity divergence is observed (Figure 5e) as expected from early work by Cromwell (1953). The observed meridional velocity trends are 57% ± 17% north of the equator (Figure 5g; red curve), and 20% ± 10% south of the equator (Figure 5g; blue curve). Such trends are expected to drive increased divergence of near-surface currents and enhanced shallow overturning circulations (e.g., enhanced equatorial upwelling, off-equatorial downwelling, and subsurface equatorward flow).

The observed interhemispheric differences in meridional and zonal velocity trends can be attributed to the spatial pattern of wind stress changes in the tropical Pacific. The trend toward stronger poleward flow north of the

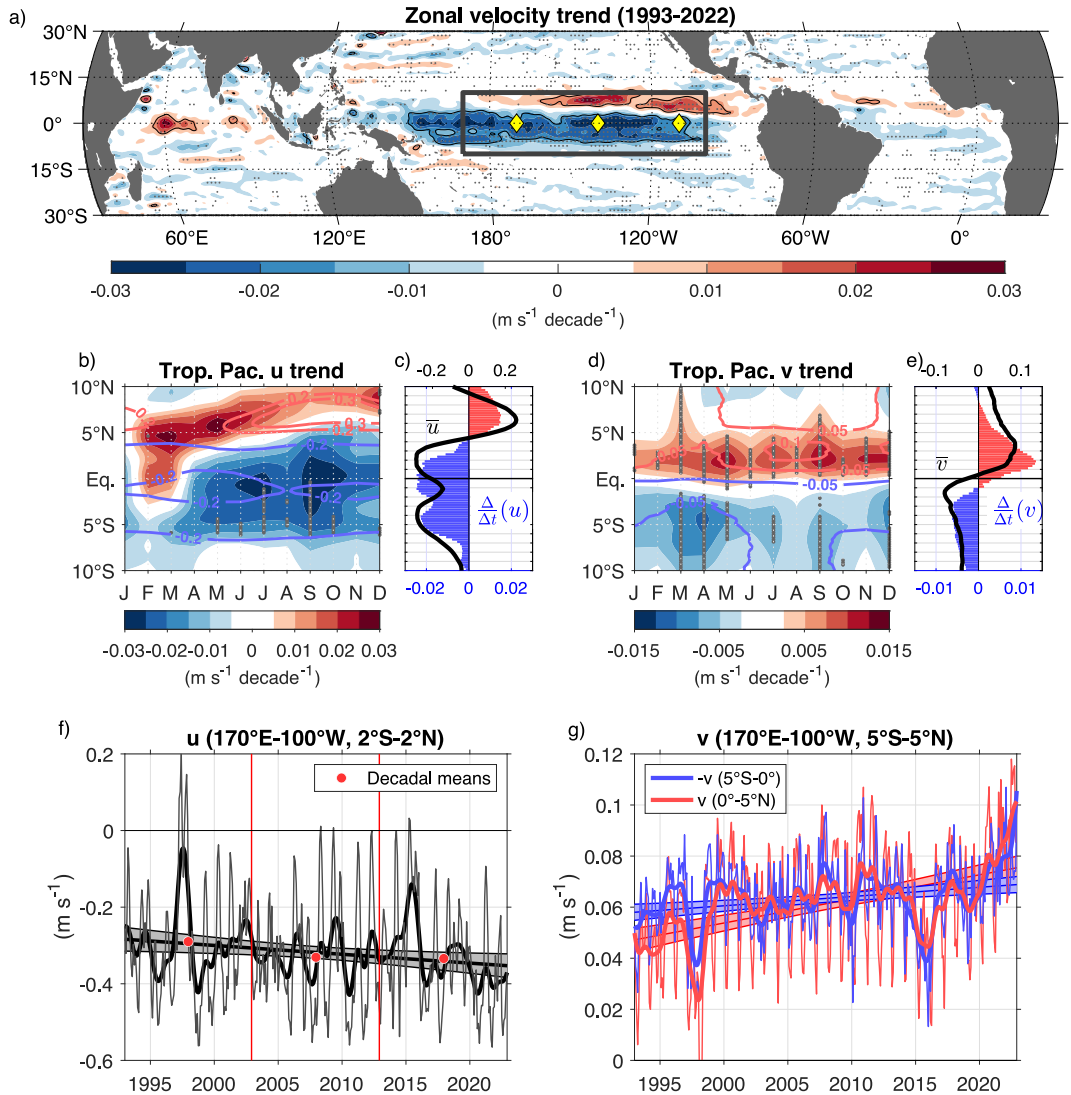

Figure 5. (a) Decadal trend of near-surface zonal velocity (u) in the tropics. Blue colors indicate negative velocity trends, while red colors indicate positive velocity trends. The tropical Pacific region (170°E−100°W, 10°S−10°N) is marked by the black box. The locations of long-term equatorial ADCP moorings as part of the TAO array at 170°W, 140°W, and 110°W are indicated by yellow diamonds. Speckled regions indicate significant zonal velocity trends at 95% confidence. (b) Decadal trend of near-surface zonal velocity (color shading) and mean zonal velocity (color contours) as a function of month and zonally averaged for the central tropical Pacific Ocean region (170°E−100°W) indicated in (a). Blue contour lines indicate mean westward velocity and red contour lines indicate mean eastward velocity (in m s^{-1}). (c) Zonally averaged (170°E−100°W) annual mean zonal velocity (black line; m s^{-1}) and annual mean decadal trend (red and blue bars; m s^{-1} $decade^{-1}$). (d) Same as (b) but for meridional velocity, v. Blue contour lines indicate mean southward velocity and red contour lines indicate mean northward velocity. Gray dots in (b) and (d) indicate significant trends at 95% confidence. (e) Same as (c) but for meridional velocity, v. (f) Monthly time series (thin curve), filtered time series (25 month running-mean; thick curve) and linear trend (thick line) of zonal velocity in the equatorial Pacific (170°E−100°W, 2°S−2°N). The thin lines and the shading in (f) indicate the 95% confidence band. The decadal means of zonal velocity (red dots) for 1993–2002, 2003–2012, and 2013–2022 are indicated. (g) Monthly time series (thin curves), filtered time series (25 month running-mean; thick curves) and linear trends (thick lines) of meridional velocity between 170°E−100°W, 5°S−0° (blue) and 170°E−100°W, 0°−5°N (red). Meridional velocity south of the equator (blue) has been inverted (positive southward) for better comparison of poleward flow. The thin lines and the shadings in (g) indicate the 95% confidence bands.

equator is due to the combined impact of intensified southerly winds near the equator, leading to increased poleward flow, and intensified easterlies, leading to northward flow north of the equator where the Coriolis force causes deflection. South of the equator, the observed zonal wind stress changes lead to increased southward flow that exceeds the northward flow contribution driven directly by increased southerly cross-equatorial winds.

Overall, the observed trends in the upper-ocean circulation agree well with the expected dynamic response to the observed wind stress changes.

In contrast to meridional velocity trends which are consistently enhancing the mean state throughout the year, zonal velocity trends near the equator display a seasonal sign reversal, with eastward velocity trends that signify a deceleration of westward currents during February and March, and accelerating westward currents during the remainder of the year (Figure 5b). Potential reasons for this trend reversal will be discussed in Section 5. Despite the seasonal reversal, the long-term annual mean strengthening of zonal and meridional velocity in the equatorial Pacific is ongoing, but modulated at interannual to decadal time scales (Figures 5f and 5g). In particular, velocity data during the most recent decade from 2013 to 2022, which was not included in England et al. (2014), are dominated by the strong El Niño event in 2015/2016 and the triple-dip La Niña event from 2020 to 2023 (Li et al., 2023), leading to an extremely strong decadal acceleration in zonal and meridional velocity (Figures 5f and 5g).

The long-term intensification of zonal near-surface currents and the steepening of the zonal SSH gradient along the equator must be balanced by intensified eastward currents near the depth of the thermocline (e.g., Yu & McPhaden, 1999b). To investigate the response of the equatorial Pacific subsurface circulation to the trends in winds and SSH at the surface, we analyze moored velocity data at 0°, 170°W, 0°, 140°W, and 0°, 110°W (locations indicated by the yellow diamonds in Figure 5a). Equatorial zonal velocity in the upper 250 m is dominated by the eastward Pacific Equatorial Undercurrent (EUC) and its seasonal intensification and shoaling (red contours in Figures 6a–6c). The EUC core velocity is defined as the maximum eastward velocity between depths of 20–200 m. The EUC peaks at 170°W in May–June at around 140 m, at 140°W in May at 100 m, and at 110°W in April–May at 70 m (Figures 6a–6c). Maximum velocities range from 0.8 m s^{-1} at 170°W to 1.3 m s^{-1} and 1.4 m s^{-1} at 110°W and 140°W, respectively. Zonal velocity trends in the upper 250 m are generally dominated by eastward trends in the upper 50–100 m and westward trends below (color shading in Figures 6a–6c,g-i). Zonal velocity trends in the western equatorial Pacific at 170°W are modest but are considerably more pronounced in the central (140°W) and eastern (110°W) Pacific. At 140°W and 110°W, eastward trends are strongest during January-March and July-December (Figures 6e and 6f) and generally above the annual mean EUC core depth (Figures 6h and 6i). During April–June, when the EUC is normally at its maximum velocity, westward trends act to reduce the seasonal peak of the EUC. The seasonality of the trends in EUC velocity and core depth (depth of maximum eastward velocity) shows that months with weaker velocities and deeper EUC core also have the strongest trends, resulting in reductions in the amplitudes of the seasonal cycles of EUC velocity and core depth (Figures 6d–6f). We observe increased eastward EUC core velocities at 170°W in January, at 140°W in February, and at 110°W in March (black solid lines in Figures 6d–6f), potentially resembling the subsurface signature of eastward propagating low-baroclinic mode Kelvin waves that will be discussed in Section 5. These trends are in alignment with near-surface zonal velocity trends from the drifter-wind-altimetry synthesis at these discrete mooring locations (black dashed lines in Figures 6d–6f), indicating a mutual near-surface and subsurface response to wave propagation.

As a consequence of the strengthening of both the upper EUC and the westward near-surface current, vertical shear of zonal velocity increased in the upper 50 m and decreased below the core of the EUC at the central and eastern equatorial Pacific mooring sites (Figures 7b and 7c). If the increased upper-ocean vertical shear overcomes the local stratification, it is a likely source for vertical mixing (W. Wang & McPhaden, 1999, 2001) and enhanced baroclinic instability driving enhanced generation of tropical instability waves (Masina et al., 1999; von Schuckmann et al., 2008), which have an impact on the mixed layer heat budget (Baturin & Niiler, 1997; Bryden & Brady, 1989; Maillard et al., 2022; Xue et al., 2020). This is in alignment with the recently reported multi-decadal intensification of Pacific tropical instability waves since the 1990s (M. Wang et al., 2024).

Overall, the Pacific EUC core shows a long-term increase of approximately 0.006 m s^{-1} $decade^{-1}$ (+2% ± 10% with respect to the mean EUC core velocity) at 170°W and about 0.02 m s^{-1} $decade^{-1}$ (+6% ± 7%) at 140°W, and a long-term decrease of −0.004 m s^{-1} $decade^{-1}$ (−1% ± 10%) at 110°W (Figures 6d–6f and 8a–8c). These EUC core velocity trends are not significant at 95% confidence and somewhat smaller than the estimate of approximately 0.07 m s^{-1} $decade^{-1}$ between 180° and 160°W by Amaya et al. (2015) who examined the time period 1990–2009. However, upper ocean zonal velocity trends (Figures 6a–6c, 6g–6i) are considerably stronger and significant at 95% confidence above the mean core depth of the EUC at all mooring sites, and as large as

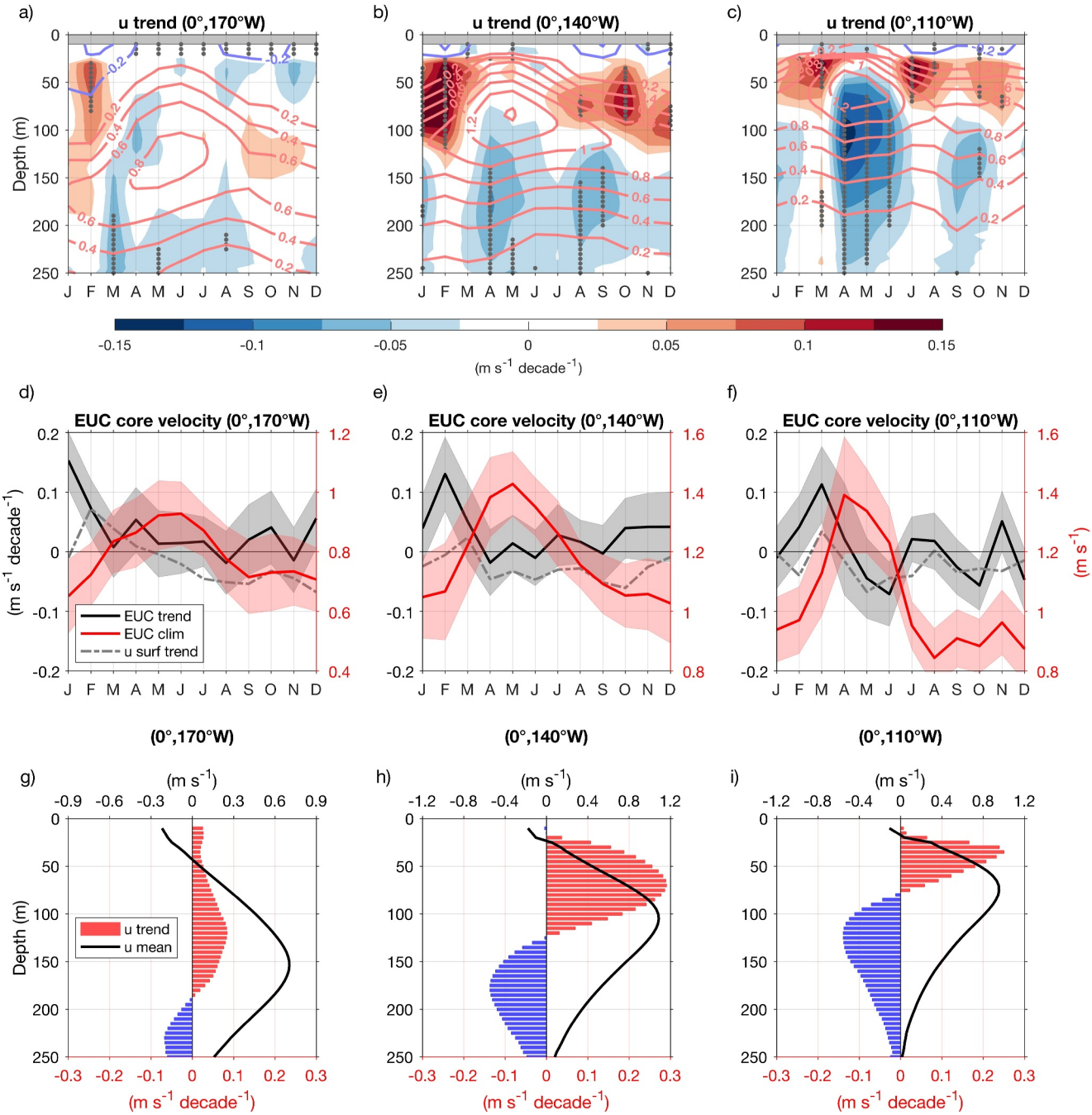

Figure 6. (a) Upper-ocean zonal velocity trends at 0°, 170°W (color shading). Gray dots indicate significant trends at 95% confidence. The red and blue contour lines indicate the climatological zonal velocity (in m s^{-1}). (b) Same as (a) but at 0°, 140°W. (c) Same as (a) but at 0°, 110°W. (d) Climatological Equatorial Undercurrent (EUC) core velocity (red curve), trend (black curve), and near-surface zonal velocity trend from the drifter-wind-altimetry product (dashed gray curve) at 0°, 170°W. (e) Same as (d) but at 0°, 140°W. (f) Same as (d) but at 0°, 110°W. The shadings in (d)–(f) indicate the 95% confidence interval (gray) and the standard error (red). (g) Vertical mean profile of zonal velocity (black curve) and zonal velocity annual mean trend (colored bars) at 0°, 170°W. Red colors indicate increased eastward velocity and blue colors indicate increased westward velocity. (h) Same as (g) but at 0°, 140°W. (i) Same as (g) but at 0°, 110°W.

0.2–0.3 m s^{-1} $decade^{-1}$ at 140°W and 110°W. The seasonal vertical migration of the EUC places its core just below the maximum zonal velocity trends (Figures 6a–6c, 6g–6i).

Besides a pure strengthening and weakening of the upper and lower EUC, respectively, the vertical movement of the EUC needs to be examined as a cause for the observed upper-ocean velocity trends. Between 1993 and 2022,

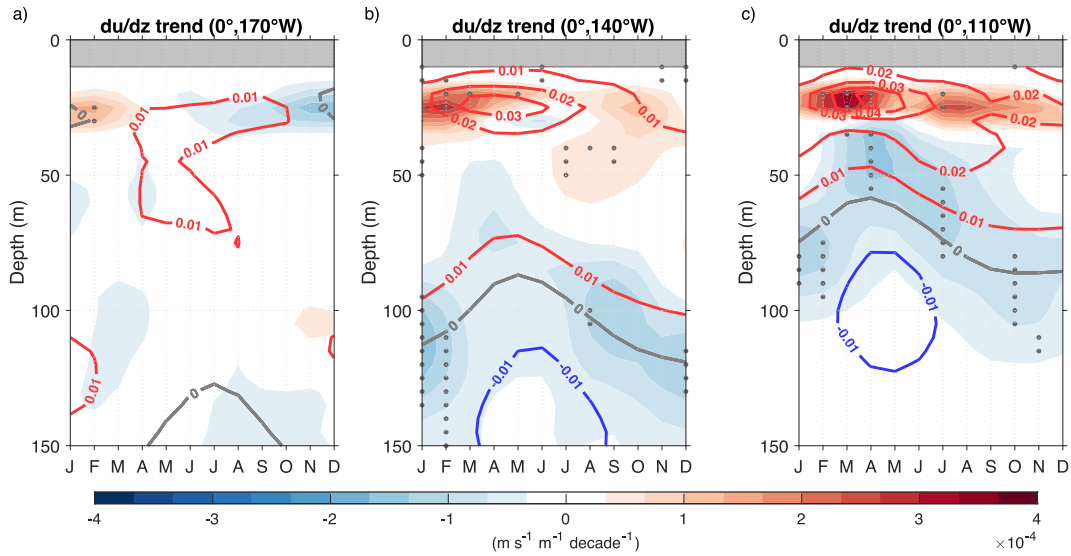

Figure 7. Upper-ocean vertical shear of zonal velocity (du/dz) trend (color shading) and du/dz mean (color contours; m s^{-1} m^{-1}) as a function of month at (a) 0°, 170°W, (b) 0°, 140°W, and (c) 0°, 110°W. Gray dots indicate significant trends at 95% confidence.

the core of the EUC deepened in the western equatorial Pacific (+6 ± 11 m at 170°W; from 140 to 146 m), while it significantly shoaled in the central equatorial Pacific (−12 ± 8 m at 140°W; from 109 to 97 m) and eastern equatorial Pacific (−12 ± 7 m at 110°W; from 78 to 66 m) (Figures 8d–8f). This trend pattern describes a basin-wide steepening of the equatorial Pacific thermocline as previously described in McPhaden et al. (2011) and Hu et al. (2013). While long-term, upper-ocean velocity data are only available at 170°W, 140°W, and 110°W, subsurface temperature data have been measured at these three moorings (Figures 8g–8i) and at six additional mooring locations along the equator (156°E, 165°W, 180°, 155°W, 125°W, 95°W; Figure 9) for the last 3 to 4 decades. For consistency, here only temperature data between 1993 and 2022 is considered. Trends in the 20°C isotherm depth at all nine locations paint a consistent picture of a deepening thermocline in the western equatorial Pacific and a shoaling thermocline in the eastern equatorial Pacific (Figure 9). Significant deepening is observed at 156°E, 165°E, 180°, and 170°W, while significant shoaling is observed at 95°W. Interestingly, the EUC core at 140°W was located below the thermocline at the beginning of the time series, but has since migrated above the thermocline during the examined time period. The fulcrum of EUC core depth (between 170°W and 140°W) is located further west than the fulcrum of the 20°C isotherm depth (between 140°W and 125°W).

We conclude that the equatorial Pacific experienced a long-term acceleration of both near-surface and subsurface currents between 1993 and 2022, in agreement with trends in zonal and meridional wind stress as well as sea surface height. To further isolate the impact of wind stress changes on the observed trends in near-surface current velocities, we analyze the Ekman component and the geostrophic component of the total velocity field separately (Figure 10). The drifter-wind-altimetry synthesis product provides both the directly wind-driven (Ekman) velocity component and the geostrophic velocity component fields separately as they are calculated individually based on reanalysis winds and satellite altimetry, respectively, using spatially varying coefficients adjusted to minimize the difference between total velocity fields and drogued drifter observations low-passed to remove tides and inertial oscillations (see also Supporting Information of Tuchen, Perez, et al., 2022 for further details). In the equatorial Pacific, both wind-induced zonal velocity changes (Figure 10a) and geostrophic zonal velocity changes (Figure 10c) contribute to the observed increase of westward currents associated with the SEC, with the westward geostrophic velocity trends maximum north of the equator and the westward Ekman velocity trends stronger south of the equator. In the equatorial Pacific region (170°E−100°W, 2°S−2°N), westward Ekman velocity significantly increased by 37% ± 10%, while westward geostrophic velocity increased by 13% ± 19%, showing a stronger contribution of the wind-driven velocity component to the overall near-surface velocity trends. However, changes in geostrophic velocity on the equator are mainly driven by changes in the zonal SSH gradient, which are also influenced by wind changes and the redistribution of water masses. Therefore, geostrophic velocity changes are expected to reflect wind changes as well. The strengthening of the NECC comes primarily from zonal

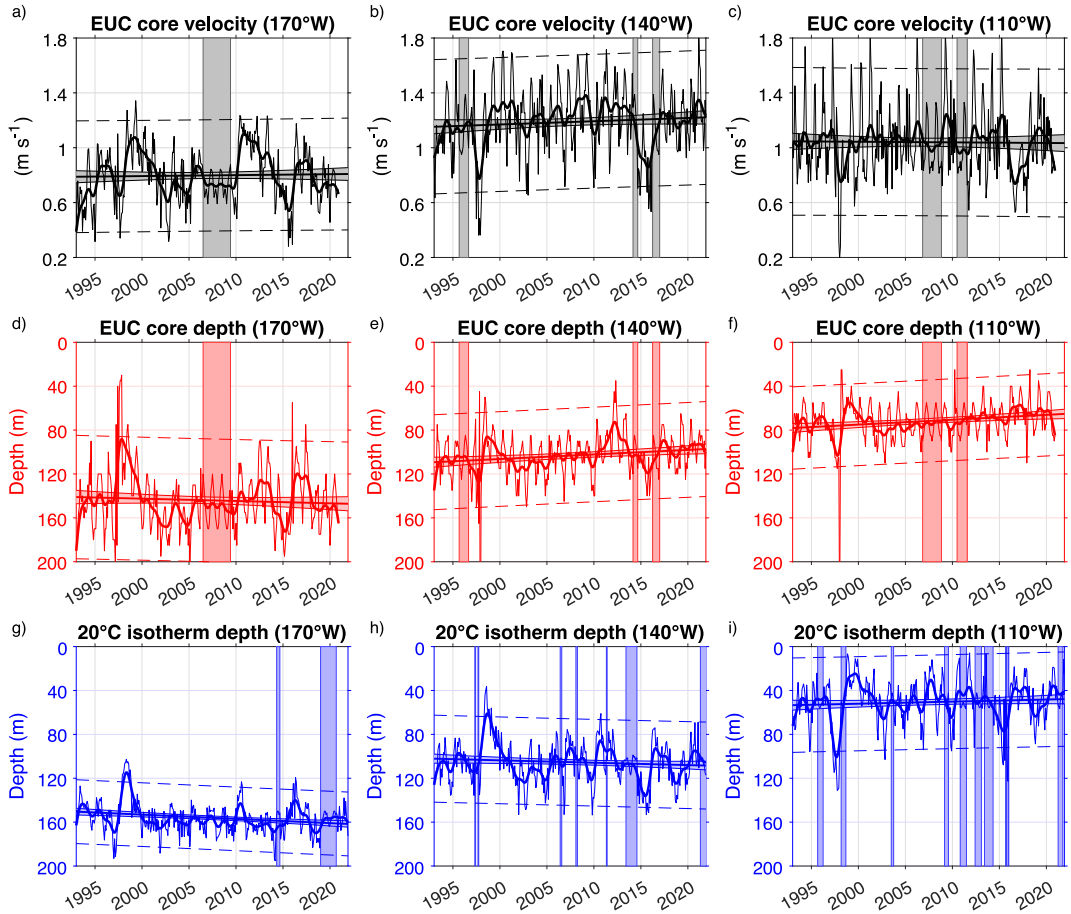

Figure 8. (a) Pacific Equatorial Undercurrent (EUC) core velocity monthly time series (thin curve) and filtered (25 month running-mean; thick curve) at 0°, 170°W. (b) Same as (a) but at 140°W. (c) Same as (a) but at 110°W. (d) Pacific EUC core depth monthly time series (thin curve) and filtered (25 month running-mean; thick curve) at 0°, 170°W. (e) Same as (d) but at 140°W. (f) Same as (d) but at 110°W. (g) Depth of the 20°C isotherm time series (thin curve) and filtered (25 month running-mean; thick curve) at 0°, 170°W. (h) Same as (g) but at 140°W. (i) Same as (g) but at 110°W. In all panels, the linear trend (thick line), the 95% confidence interval (thin lines and shading), and the 95% prediction interval (dashed lines) are indicated. Time periods with no data are filled by climatological values and indicated by color shaded rectangles.

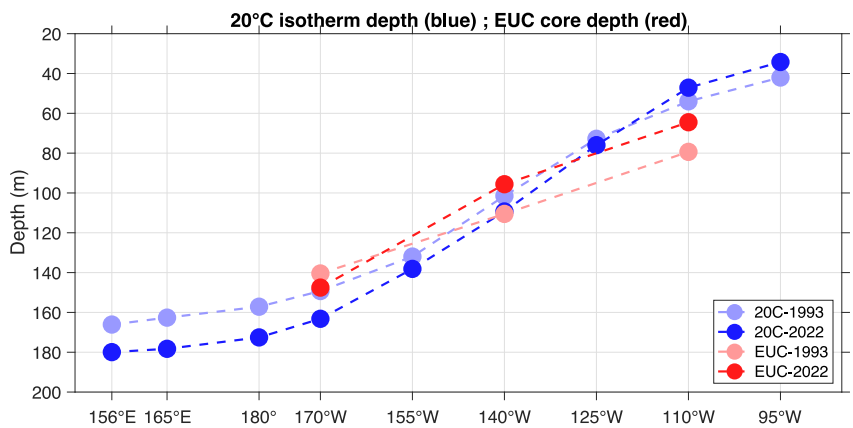

Figure 9. Pacific EUC core depth (red) and 20°C isotherm depth (blue) changes between 1993 and 2022. Shown are the start (January 1993; light colors) and end points (December 2022; dark colors) of the linear trend lines from the monthly time series at each equatorial mooring site.

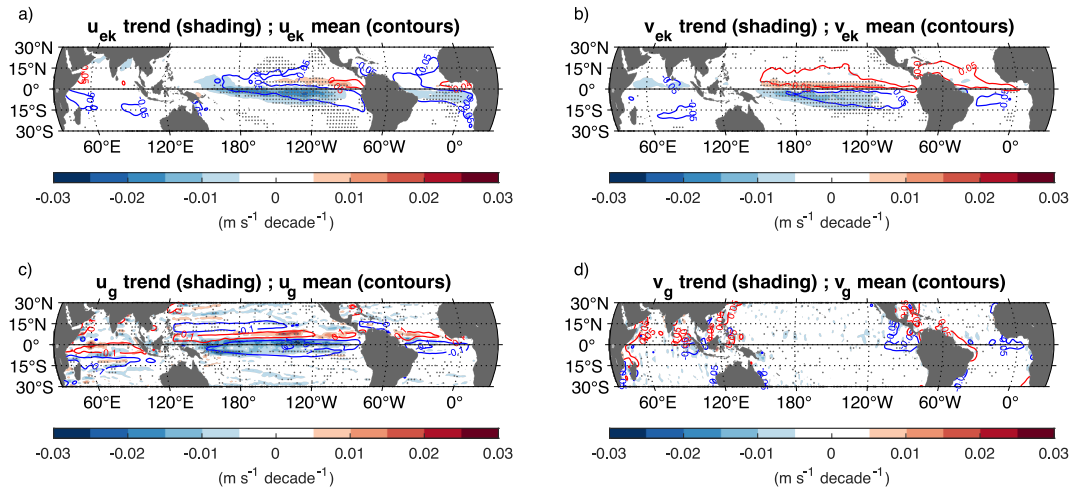

Figure 10. (a) Wind-driven (Ekman) zonal velocity trends in the tropics. Blue shadings (contours) indicate westward velocity anomalies (mean westward velocity), while red shadings (contours) indicate eastward velocity anomalies (mean eastward velocity). (b) Wind-driven (Ekman) meridional velocity trend in the tropics. Blue shadings (contours) indicate southward velocity anomalies (mean southward velocity), while red shadings (contours) indicate northward velocity anomalies (mean northward velocity). (c) Same as (a) but for geostrophic zonal velocity. (d) Same as (b) but for geostrophic meridional velocity. The ±0.05 m s^{-1} contour lines are indicated in (a), (b) and (d). The ±0.1 m s^{-1} contour lines are indicated in (c). Speckled regions indicate significant trends at 95% confidence.

geostrophic velocity changes, and secondarily from wind-driven geostrophic velocity changes (Figures 10a and 10c). Meridional velocity changes are primarily caused by wind-driven (Ekman) velocity changes (Figures 10b and 10d). Mean meridional Ekman velocities describe the surface branches of the subtropical and tropical cells in both the tropical Pacific and Atlantic (cf., Johnson, 2001; Perez et al., 2014; Schott et al., 2004; Tuchen et al., 2019, 2020; Tuchen, Brandt, et al., 2022), but only meridional Ekman velocities near the equatorial Pacific exhibit a significant intensification (Figure 10b): in the northern hemisphere (170°E−100°W, 0°−5°N) northward Ekman velocity increased by 42% ± 12%, while in the southern hemisphere (170°E−100°W, 5°S−0°) southward Ekman velocity increased by 15% ± 8%. Hence, we conclude that the near-equatorial buildup of meridional velocity trends primarily reflects an acceleration of the tropical cells, while the subtropical cells remain largely unaffected. This is in agreement with previous studies showing that the subtropical cells are unaffected by equatorial winds and mainly respond to subtropical winds (e.g., Graffino et al., 2019).

5. Discussion and Conclusions

In this study, we present observational evidence for an ongoing (from 1993 to 2022) intensification of equatorial Pacific winds and upper-ocean currents, as well as a steepening zonal sea surface height gradient and equatorial thermocline. Additionally, we provide novel insights regarding the seasonality and interannual to decadal modulation that are superimposed on the observed trends. The main new findings of this study are.

- Between 1993 and 2022, there was a sustained increase of tropical Pacific southeasterly trade winds, but this increase is strongly modulated by interannual and decadal variations. While southerly winds intensification is more pronounced north of the equator, easterly wind trends are stronger south of the equator. Although increasing winds are observed throughout the year, the most pronounced trends are observed from boreal autumn to winter.
- Multi-decadal intensification of equatorial Pacific near-surface currents is observed from a synthesis product using drifter velocities, reanalysis winds, and satellite altimetry. Throughout the majority of the year, westward near-surface currents exhibit a remarkable intensification of 19%, yet a distinct reduction was observed during the months of February to March.
- Subsurface zonal velocities from mooring data displayed a substantial intensification in the central and eastern Pacific. The Pacific EUC core became shallower in the central and eastern Pacific, while it deepened in the western Pacific. However, most of the intensification occurs above the depth of the EUC core leading to increased upper-ocean vertical shear.

- The increases of equatorial Pacific near-surface and subsurface currents are in line with previous studies that utilized in-situ and reanalysis data (Amaya et al., 2015; Drenkard & Karnauskas, 2014; M. Wang et al., 2024; Yang et al., 2014). However, we find smaller trends for the Pacific EUC core velocity, likely because the earlier studies predate strong interannual variations observed between 2011 and 2022 (e.g., Figures 10b and 10c) and because the strongest zonal velocity trends are observed above the depth of the EUC core and hence not reflected in EUC core velocity trends. As a consequence of the shoaling EUC core and the intensifying westward flow near the surface, the vertical shear of zonal velocity increased above the EUC core. This could be associated with potentially intensified vertical mixing and upper-ocean cooling at the equator.
- Subsurface temperature measurements from moorings provide evidence of a substantial steepening of the equatorial Pacific thermocline. A shallower thermocline in the eastern equatorial Pacific is associated with a decrease of ENSO amplitude in the eastern Pacific and a trend toward more frequent central Pacific El Niños than eastern Pacific El Niños (e.g., Hu et al., 2013; McPhaden et al., 2011).
- Zonal velocity trends arise mainly from changes in the wind-driven velocity component, but changes in the geostrophic velocity component contribute as well.
- Wind-driven changes dominate trends in meridional velocity associated with the poleward flow of the tropical cells. In particular, near-equatorial poleward flow in the northern hemisphere has intensified significantly by 57%, while southern hemisphere poleward flow shows a modest increase of 20%. Meridional velocity trends are confined to the equatorial region, ruling out the possibility that the observed trends are caused by an acceleration of the subtropical cells. The increased meridional divergence over the past three decades implies increased equatorial upwelling which will be examined in future research.

While zonal winds intensified consistently throughout the year, trends in the near-surface currents display a distinct seasonality, with eastward velocity trends during February to March. The observed seasonality in zonal velocity trends is consistent with findings from the analysis of Ocean Surface Current Analysis Real-time (OSCAR) (ESR, 2009) data, ECMWF-ORAS5 reanalysis data (Copernicus, 2021) and AVISO geostrophic velocities (Copernicus, 2023) (not shown). Local wind forcing can be ruled out as the main contributor to the seasonality of the circulation trends, as zonal wind stress trends are consistently negative, tending to accelerate westward currents near the equator throughout the year (Figure 2b). Instead, equatorial Pacific sea surface height (SSH) holds the key to interpreting the seasonal velocity trends.

In general, enhanced zonal winds induce anomalous westward mass transport, leading to an increased zonal SSH gradient (Figure 4). The steepening trend of the equatorial SSH slope is seasonally dependent and is substantially less pronounced during February and March, when positive SSH trends expand far into the central and eastern equatorial basin (Figure 11b). This eastward expansion resembles an eastward propagation of trends in SSH anomalies from January to March. During boreal summer (July-September), mean negative wind stress curl north of the equator near 180° intensified (Figure S2 in Supporting Information S1) which is a likely source of increased Rossby wave activity. Rossby waves propagate westward and continue as coastally trapped waves along the western boundary before reflecting eastward at the equator into Kelvin waves (Suarez & Schopf, 1988). We remove the annual mean SSH trend for each longitude (Figure 11) and examine the anomalous SSH trends north of the equator (3°N−8°N; Figure 11a) and near the equator (2°S−2°N; Figure 11b). It shows that the north equatorial region is dominated by westward propagation of positive SSH trends with a phase speed of about 0.5 m s^{-1} (Figure 11a), consistent with a first meridional mode equatorially trapped Rossby wave in the presence of meridionally sheared equatorial flow (Chelton et al., 2003), which are seemingly reflected at the western boundary into eastward propagating Kelvin waves with propagation speed of approximately 1.9 m s^{-1} (Figure 11b). This latter speed is consistent with a combination of first and second baroclinic mode equatorial Kelvin waves. These findings are also in alignment with Yu and McPhaden (1999a), who noted a boreal spring reversal of the mean westward SEC in the eastern equatorial Pacific due to equatorial wave activity. However, here we report on changing Kelvin wave activity that manifests as a 30 year trend seasonally phase-locked to boreal winter/spring. The corresponding zonal velocity trend aligns with the observed SSH trend (Figure 11; contour lines): positive SSH trend anomalies north of the equator are associated with westward velocity trends (Figure 11a), while positive SSH trend anomalies at the equator are associated with eastward velocity trends (Figure 11b).

To show that the equatorial trends are not caused by isolated extreme events at the beginning and/or toward the end of the time series, we analyze equatorial SSH anomalies averaged during February and March for each year from 1993 to 2022 (Figure S3a in Supporting Information S1). Equatorial downwelling (upwelling) Kelvin waves

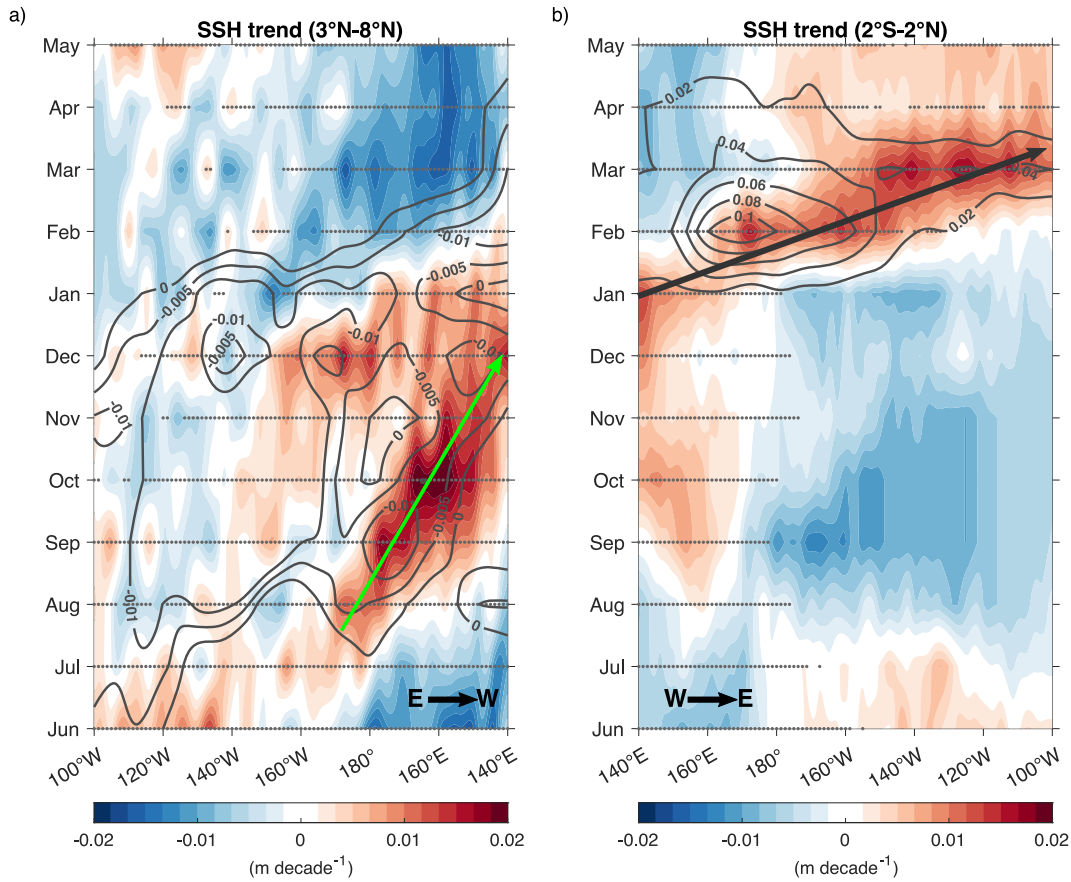

Figure 11. (a) Monthly SSH trend anomalies averaged between 3°N and 8°N. Note that the longitude axis is reversed showing east to west. The green arrow indicates a best-fit westward propagation with a phase speed of about 0.5 m s^{-1}. (b) Monthly SSH trend anomalies averaged between 2°S and 2°N. The solid black arrow indicates a best-fit eastward propagation with a phase speed of about 1.9 m s^{-1}. Contour lines in (a) and (b) show zonal velocity trends (in m s^{-1} $decade^{-1}$). The annual mean SSH trend and the annual mean zonal velocity trend (3°N−8°N in (a), and 2°S−2°N in (b)) have been subtracted to yield trend anomalies. Gray dots indicate significant SSH trend anomalies at 95% confidence.

are characterized by positive (negative) SSH anomalies as they deepen (shoal) the equatorial thermocline. In particular, El Niño (La Niña) events are triggered by downwelling (upwelling) Kelvin waves. Hence, interannual variability due to ENSO dominates equatorial SSH anomalies during February to March. Overall, positive SSH anomalies (downwelling Kelvin waves) became stronger and more frequent between 1993 and 2022 (Figure S4 in Supporting Information S1). The time series is dominated by negative SSH anomalies between 1998 and 2002 and by positive SSH anomalies between 2014 and 2022. In particular, 2014 and 2015 exhibit pronounced positive SSH anomalies in the western equatorial Pacific that are exceeding the underlying long-term trend. Equatorial zonal velocity anomalies averaged during February and March for each year correlate significantly ($r > 0.6$; $p < 0.05$) with SSH anomalies in the western equatorial Pacific between 170°E to 170°W (Figure S3b in Supporting Information S1). The time period 1993–2022 encompasses a major shift in the PDO from positive to negative at the beginning of the 21st century (McPhaden & Zhang, 2002, 2004). We repeat the calculations for Figure 11 but exclude the years 1997–2002 (Figure S5 in Supporting Information S1) and find that our results hold: increased off-equatorial and equatorial wave propagation is occurring during February and March. We conclude that the seasonal reversal of zonal near-surface velocity trends during February and March is most likely due to a combination of (a) a multidecadal trend toward more frequent, positive SSH anomalies and (b) interannual variability due to ENSO and variability on decadal to multidecadal time scales that may be an imprint of ENSO modulation and/or changes in ENSO diversity on these time scales.

One major finding of this study is that the equatorial thermocline has steepened over the last 30 years. While the western equatorial Pacific thermocline is about 20 m deeper than 30 years ago, the eastern equatorial Pacific

thermocline shoaled by about 12 m during the same time period. El Niño events are usually excited by a series of air-sea interactions. The Bjerknes feedback (Bjerknes, 1969) describes how SST anomalies in the eastern basin are forced by thermocline depth anomalies due to eastward propagating Kelvin waves. A shallower thermocline in the eastern equatorial Pacific, and a steeper slope of the equatorial thermocline in general, is expected to decrease ENSO amplitude as shown in sensitivity experiments (Hu et al., 2013). In particular, the combined effect of thermocline shoaling and increased southeasterly trade winds has been shown to hinder the eastward propagation of warm water during an El Niño event (Hu et al., 2013). In addition, the recently reported increase in tropical instability wave activity over the recent three decades (M. Wang et al., 2024) could add to the damping effect on ENSO, as tropical instability waves have a mean cooling effect on the equator through meridional temperature advection and vertical mixing (e.g., Maillard et al., 2022; Xue et al., 2020, 2021). Hence, the observed thermocline steepening could counteract any potential long-term trends in El Niño intensity and/or frequency.

Beyond the described long-term increases of winds and currents, these parameters have undergone considerable modulation on interannual to decadal timescales over the past three decades. By extending the time period analyzed by England et al. (2014), we find that winds and currents underwent a declining phase between 2010 and 2016, but subsequently rebounded to positive trends past 2016. This particular period was dominated by the strong El Niño event in 2015/16 and the triple-dip La Niña from 2020 to 2023, which are superimposed on the decadal trends.

Our findings highlight the role that wind changes have on the equatorial Pacific upper-ocean circulation. England et al. (2014) quantified the impact of tropical Pacific winds on global surface air temperature (SAT) using three different future scenarios: persistence, stabilization, or reversal of tropical Pacific wind trends after 2012. Their model experiment revealed that the disparity between persistent and reversing wind trends amounts to a difference of approximately 0.15°C of global SAT, indicating a substantial impact on the global climate system. Despite continued wind trends, global mean temperature has rapidly increased over the past 10 years. By examining an additional decade of data, we provide observational evidence for the persistence of wind trends and their continued effects on upper-ocean currents, as well as their dynamical impact on the distribution of SST.

The majority of state-of-the-art coupled climate models are not able to reproduce the observed trends in tropical South Pacific cooling, raising questions about their ability to accurately project future trends and multidecadal variability in SST (Heede & Fedorov, 2023; Latif et al., 2023). Recent studies suggest that both model bias and natural variability are the reason for the model's inaccurate representation of the observed trends (Bai et al., 2023; Lee et al., 2022; Wills et al., 2022). In particular, the models' misrepresentation of easterly trade wind trends, subsurface cooling, and cold tongue extension lead to a weaker than observed SST zonal gradient (Bai et al., 2023). A slow down or reversal of Pacific wind trends in response to a phase change of the IPO and/or PDO could accelerate the rise of global mean temperature even more. However, the relative contributions of natural variability and external forcing to the observed SST trend pattern are still under debate. Recently, another pattern extracted from the observed SST trend, the so-called Northern Hemisphere-Indo-West Pacific warming pattern (Heede & Fedorov, 2023), was suggested to contribute to the strengthening of the Pacific Walker circulation, in addition to the PDO and the spatially uniform externally forced warming trend. Furthermore, we emphasize the contribution of tropical Pacific Ocean dynamics to global-scale climate variations and trends in SST. Future research will also focus on conducting a comprehensive analysis of the heat budget to quantify the relative roles of ocean dynamics and surface heat fluxes in the observed long-term cooling trend in the tropical South Pacific.

This study may further serve as a valuable benchmark to validate the representation of mean currents and their long-term trends in model simulations and reanalysis products (e.g., Karnauskas et al., 2020). In analogy to how models and reanalysis products represent the observed tropical Pacific SST trends, experiments can be designed to understand potential discrepancies in upper-ocean circulation between simulations and observations, in particular improved representation of vertical processes such as equatorial upwelling and mixing (e.g., Iyer & Moum, 2024; Moum et al., 2022). Based on the observed changes in near-surface zonal and meridional velocity, future research will focus on the analysis of near-surface upwelling trends, inferred from horizontal current divergence. Observing and understanding equatorial upwelling will be crucial as it plays a significant role in regulating the equatorial Pacific cold tongue region (180°–80°W, 3°S–3°N) (Clement et al., 1996) and provides physical and biogeochemical background conditions for marine ecosystems (Chavez et al., 1999; Deutsch et al., 2014; Frankemölle et al., 2024). While global warming is projected to weaken equatorial Pacific upwelling (L.-C. Wang et al., 2022), natural variability may episodically counteract these externally forced effects.

Data Availability Statement

All satellite observations and reanalysis data used in this analysis are publicly available: NOAA OI SST V2.1 High Resolution Dataset data provided by the NOAA PSL, Boulder, Colorado, USA, from their website at https://psl.noaa.gov (Huang et al., 2021), CMEMS-C3S-SLA version DT2021 (Copernicus, 2023), ECMWF ERA5 hourly 10 m horizontal wind speed (Hersbach et al., 2020, 2023), GPCP monthly precipitation data version 3.2 (Huffman et al., 2022), OSCAR ocean surface currents (ESR, 2009), ECMWF ORAS5 reanalysis data (Copernicus, 2021). The near-surface drifter-wind-altimetry synthesis data can be accessed at https://www.aoml.noaa.gov/ftp/pub/phod/lumpkin/decomp/. Data obtained by tropical Pacific moored surface buoys are made available by the GTMBA Project Office of NOAA/PMEL at https://www.pmel.noaa.gov/tao/drupal/disdel/.

Acknowledgments

We thank Kandaga Pujiana and three anonymous reviewers for helpful comments and suggestions on the manuscript. This research was supported in part by an appointment to the NRC Research Associateship Program at NOAA's Atlantic Oceanographic and Meteorological Laboratory (AOML), administered by the Fellowships Office of the National Academies of Sciences, Engineering, and Medicine. This research was carried out in part under the auspices of the Cooperative Institute for Marine and Atmospheric Studies (CIMAS), a Cooperative Institute of the University of Miami and NOAA, cooperative agreement # NA20OAR4320472. RCP and GRF were supported by NOAA's Global Ocean Monitoring and Observing (GOMO) Program (funding reference number 100007298), under the PIRATA Northeast Extension project. MJM acknowledges support by NOAA's Pacific Marine Environmental Laboratory (PMEL) and funding by NOAA's GOMO Global Tropical Moored Buoy Array (GTMBA) project. PMEL contribution no. 5596. FPT, RCP, GRF, and RL acknowledge support by NOAA's AOML. RL was supported by GOMO Global Drifter Program funding. Moored velocity observations were acquired by the Tropical Atmosphere Ocean (TAO) program supported by NOAA.

References

Adler, R. F., Gu, G., Sapiano, M., Wang, J.-J., & Huffman, G. J. (2017). Global precipitation: Means, variations and trends during the satellite era (1979–2014). *Surveys in Geophysics*, *38*, 679–699. https://doi.org/10.1007/s10712-017-9416-4

Amaya, D. J., Xie, S.-P., Miller, A. J., & McPhaden, M. J. (2015). Seasonality of tropical Pacific decadal trends associated with the 21st century global warming hiatus. *Journal of Geophysical Research: Oceans*, *120*(10), 6782–6798. https://doi.org/10.1002/2015JC010906

An, S.-I., Kim, J.-W., Im, S.-H., Kim, B.-M., & Park, J.-H. (2012). Recent and future sea surface temperature trends in tropical Pacific warm pool and cold tongue regions. *Climate Dynamics*, *39*, 1373–1383. https://doi.org/10.1007/s00382-011-1129-7

Bai, W., Liu, H., Lin, P., Li, X., & Wang, F. (2023). Reconciling opposite trends in the observed and simulated equatorial Pacific zonal sea surface temperature gradient. *Geoscience Letters*, *10*, 56. https://doi.org/10.1186/s40562-023-00309-3

Baturin, N. G., & Niiler, P. P. (1997). Effects of instability waves in the mixed layer of the equatorial Pacific. *Journal of Geophysical Research*, *102*(C13), 27771–27793. https://doi.org/10.1029/97JC02455

Bjerknes, J. (1969). Atmospheric teleconnections from the equatorial Pacific. *Monthly Weather Review*, *97*(3), 163–172. https://doi.org/10.1175/1520-0493(1969)097<0163:ATFTEP>2.3.CO;2

Bond, N. A., Overland, J. E., Spillane, M., & Stabeno, P. (2003). Recent shifts in the state of the North Pacific. *Geophysical Research Letters*, *30*(23), 2183. https://doi.org/10.1029/2003GL018597

Brandt, P., Alory, G., Awo, F. M., Dengler, M., Djakouré, S., Imbol Koungue, R. A., et al. (2023). Physical processes and biological productivity in the upwelling regions of the tropical Atlantic. *Ocean Science*, *19*(3), 581–601. https://doi.org/10.5194/os-19-581-2023

Brandt, P., Hahn, J., Schmidtko, S., Tuchen, F. P., Kopte, R., Kiko, R., et al. (2021). Atlantic Equatorial Undercurrent intensification counteracts warming-induced deoxygenation. *Nature Geoscience*, *14*(5), 278–282. https://doi.org/10.1038/s41561-021-00716-1

Bryden, H. L., & Brady, E. C. (1989). Eddy momentum and heat fluxes and their effects on the circulation of the equatorial Pacific Ocean. *Journal of Marine Research*, *47*(1), 55–79. Retrieved from https://elischolar.library.yale.edu/journal_of_marine_research/1922/

Capotondi, A., McGregor, S., McPhaden, M. J., Cravatte, S., Holbrook, N. J., Imada, Y., et al. (2023). Mechanisms of tropical Pacific decadal variability. *Nature Reviews Earth & Environment*, *4*(11), 754–769. https://doi.org/10.1038/s43017-023-00486-x

Capotondi, A., & Qiu, B. (2023). Decadal variability of the Pacific shallow overturning circulation and the role of local wind forcing. *Journal of Climate*, *36*(3), 1001–1015. https://doi.org/10.1175/JCLI-D-22-0408.1

Chavez, F. P., Strutton, P. G., Friederich, G. E., Feely, R. A., Feldman, G. C., Foley, D. G., & McPhaden, M. J. (1999). Biological and chemical response of the equatorial Pacific Ocean to the 1997-98 El Niño. *Science*, *286*(5447), 2126–2131. https://doi.org/10.1126/science.286.5447.2126

Chelton, D. B., Schlax, M. G., Lyman, J. M., & Johnson, G. C. (2003). Equatorially trapped Rossby waves in the presence of meridionally sheared baroclinic flow in the Pacific Ocean. *Progress in Oceanography*, *56*(2), 323–380. https://doi.org/10.1016/S0079-6611(03)00008-9

Cheng, L., Abraham, J., Trenberth, K. E., Boyer, T., Mann, M. E., Zhu, J., et al. (2024). New record ocean temperatures and related climate indicators in 2023. *Advances in Atmospheric Sciences*, *41*(6), 1068–1082. https://doi.org/10.1007/s00376-024-3378-5

Clement, A. C., Seager, R., Cane, M. A., & Zebiak, S. E. (1996). An Ocean dynamical thermostat. *Journal of Climate*, *9*(9), 2190–2196. https://doi.org/10.1175/1520-0442(1996)009<2190:AODT>2.0.CO;2

Copernicus. (2021). ORAS5 global ocean reanalysis monthly data from 1958 to present [Dataset]. *Copernicus Climate Change Service (C3S) Climate Data Store (CDS)*. https://doi.org/10.24381/cds.67e8eeb7

Copernicus. (2023). Sea level daily gridded data from satellite observations for the global ocean from 1993 to present [Dataset]. *Copernicus Climate Change Service (C3S) Climate Data Store (CDS)*. https://doi.org/10.24381/cds.4c328c78

Cromwell, T. (1953). Circulation in a meridional plane in the Central Equatorial Pacific. *Journal of Marine Research*, *12*(2), 196–213. https://elischolar.library.yale.edu/journal_of_marine_research/793

Deutsch, C., Berelson, W., Thunell, R., Weber, T., Tems, C., McManus, J., et al. (2014). Centennial changes in North Pacific anoxia linked to tropical trade winds. *Science*, *345*(6197), 665–668. https://doi.org/10.1126/science.1252332

Di Lorenzo, E., Schneider, N., Cobb, K. M., Franks, P. J. S., Chhak, K., Miller, A. J., et al. (2008). North Pacific Gyre Oscillation links ocean climate and ecosystem change. *Geophysical Research Letters*, *35*(8), L08607. https://doi.org/10.1029/2007GL032838

Drenkard, E. J., & Karnauskas, K. B. (2014). Strengthening of the Pacific Equatorial Undercurrent in the SODA reanalysis: Mechanisms, ocean dynamics, and implications. *Journal of Climate*, *27*(6), 2405–2416. https://doi.org/10.1175/JCLI-D-13-00359.1

England, M. H., McGregor, S., Spence, P., Meehl, G. A., Timmermann, A., Cai, W., et al. (2014). Recent intensification of wind-driven circulation in the Pacific and the ongoing warming hiatus. *Nature Climate Change*, *4*(3), 222–227. https://doi.org/10.1038/nclimate2106

ESR. (2009). Oscar third degree resolution ocean surface currents [Dataset]. *PO.DAAC, CA, USA*. https://doi.org/10.5067/oscar-03d01

Frankemölle, P. F. V. W., Nooteboom, P. D., Scutt Phillips, J., Escalle, L., Nicol, S., & van Sebille, E. (2024). Assessing the drift of fish aggregating devices in the tropical Pacific Ocean. *Ocean Science*, *20*(1), 31–41. https://doi.org/10.5194/os-20-31-2024

Fu, S., Hu, S., Zheng, X.-T., McMonigal, K., Larson, S., & Tian, Y. (2024). Historic changes in wind-driven ocean circulation drive pattern of Pacific warming. *Nature Communications*, *15*(1), 1562. https://doi.org/10.1038/s41467-024-45677-2

GISTEMP Team. (2024). GISS Surface Temperature Analysis (GISTEMP), version 4 [Dataset]. NASA Goddard Institute for Space Studies. Retrieved from https://data.giss.nasa.gov/gistemp/

Graffino, G., Farneti, R., Kucharski, F., & Molteni, F. (2019). The effect of wind stress anomalies and location in driving Pacific subtropical cells and tropical climate. *Journal of Climate*, *32*(5), 1641–1660. https://doi.org/10.1175/JCLI-D-18-0071.1

Heede, U. K., & Fedorov, A. V. (2023). Colder eastern equatorial Pacific and stronger Walker circulation in the early 21st century: Separating the forced response to global warming from natural variability. *Geophysical Research Letters*, *50*(3), e2022GL101020. https://doi.org/10.1029/2022GL101020

Henley, B. J., Gergis, J., Karoly, D. J., Power, S., Kennedy, J., & Folland, C. K. (2015). A tripole index for the interdecadal Pacific oscillation. *Climate Dynamics*, *45*, 3077–3090. https://doi.org/10.1007/s00382-015-2525-1

Hersbach, H., Bell, B., Berrisford, P., Biavati, G., Horányi, A., Muñoz Sabater, J., et al. (2023). ERA5 hourly data on single levels from 1940 to present. *Copernicus Climate Change Service (C3S) Climate Data Store (CDS)*. https://doi.org/10.24381/cds.adbb2d47

Hersbach, H., Bell, B., Berrisford, P., Hirahara, S., Horányi, A., Muñoz-Sabater, J., et al. (2020). The ERA5 global reanalysis. *Quarterly Journal of the Royal Meteorological Society*, *146*(730), 1999–2049. https://doi.org/10.1002/qj.3803

Hu, S., & Fedorov, A. V. (2018). Cross-equatorial winds control El Niño diversity and change. *Nature Climate Change*, *8*(9), 798–802. https://doi.org/10.1038/s41558-018-0248-0

Hu, S., Sprintall, J., Guan, C., McPhaden, M. J., Wang, F., Hu, D., & Cai, W. (2020). Deep-reaching acceleration of global mean ocean circulation over the past two decades. *Science Advances*, *6*(eaax7727). https://doi.org/10.1126/sciadv.aax7727

Hu, Z.-Z., Kumar, A., Ren, H.-L., Wang, H., L'Heureux, M., & Jin, F.-F. (2013). Weakened interannual variability in the tropical Pacific Ocean since 2000. *Journal of Climate*, *26*(8), 2601–2613. https://doi.org/10.1175/JCLI-D-12-00265.1

Huang, B., Liu, C., Banzon, V., Freeman, E., Graham, G., Hankins, B., et al. (2021). Improvements of the Daily Optimum Interpolation Sea Surface Temperature (DOISST) version 2.1. *Journal of Climate*, *34*(8), 2923–2939. https://doi.org/10.1175/JCLI-D-20-0166.1

Huffman, G. J., Behrangi, A., Bolvin, D. T., & Nelkin, E. J. (2022). GPCP Version 3.2 Satellite-Gauge Combined Precipitation Data Set. *Goddard Earth Sciences Data and Information Services Center (GES DISC)*. https://doi.org/10.5067/MEASURES/GPCP/DATA304

Iyer, S., & Moum, J. N. (2024). Turbulence from tropical instability waves in the equatorial cold tongues: Quantification from multiyear moored records. *Journal of Geophysical Research: Oceans*, *129*(4), e2023JC020646. https://doi.org/10.1029/2023JC020646

Johnson, G. C. (2001). The Pacific Ocean Subtropical cell surface limb. *Geophysical Research Letters*, *28*(9), 1771–1774. https://doi.org/10.1029/2000GL012723

Karnauskas, K. B., Jakoboski, J., Johnston, T. M. S., Owens, W. B., Rudnick, D. L., & Todd, R. E. (2020). The Pacific Equatorial Undercurrent in three generations of global climate models and glider observations. *Journal of Geophysical Research: Oceans*, *125*(11), e2020JC016609. https://doi.org/10.1029/2020JC016609

Kopte, R., Brandt, P., Claus, M., Greatbatch, R. J., & Dengler, M. (2018). Role of equatorial basin-mode resonance for the seasonal variability of the Angola current at 11°S. *Journal of Physical Oceanography*, *48*(2), 261–281. https://doi.org/10.1175/JPO-D-17-0111.1

Kosaka, Y., & Xie, S.-P. (2013). Recent global-warming hiatus tied to equatorial Pacific surface cooling. *Nature*, *501*(7467), 403–407. https://doi.org/10.1038/nature12534

Latif, M., Bayr, T., Kjellson, J., Lübbecke, J. F., Martin, T., Nnamchi, H. C., et al. (2023). Strengthening atmospheric circulation and trade winds slowed tropical Pacific surface warming. *Communications Earth and Environment*, *4*(249), 249. https://doi.org/10.1038/s43247-023-00912-4

Latif, M., Kleeman, R., & Eckert, C. (1997). Greenhouse warming, decadal variability, or El Niño? An attempt to understand the anomalous 1990s. *Journal of Climate*, *10*(9), 2221–2239. https://doi.org/10.1175/1520-0442(1997)010<2221:GWDVOE>2.0.CO;2

Lee, S., L'Heureux, M., Wittenberg, A. T., Seager, R., O'Gorman, P. A., & Johnson, N. C. (2022). On the future zonal contrasts of equatorial Pacific climate: Perspectives from Observations, Simulations, and Theories. *npj Climate and Atmospheric Science*, *5*(1), 82. https://doi.org/10.1038/s41612-022-00301-2

Lenssen, N. J. L., Schmidt, G. A., Hansen, J. E., Menne, M., Persin, A., Ruedy, R., & Zyss, D. (2019). Improvements in the GISTEMP uncertainty model. *Journal of Geophysical Research: Atmosphere*, *124*(12), 6307–6326. https://doi.org/10.1029/2018JD029522

Li, X., Hu, Z.-Z., McPhaden, M. J., Zhu, C., & Liu, Y. (2023). Triple-Dip La Niñas in 1998-2001 and 2020-2023: Impact of mean state changes. *Journal of Geophysical Research: Atmospheres*, *128*(17), e2023JD038843. https://doi.org/10.1029/2023JD038843

Lumpkin, R., & Garzoli, S. (2011). Interannual to decadal changes in the western South Atlantic's surface circulation. *Journal of Geophysical Research*, *116*(C1), C01014. https://doi.org/10.1029/2010JC006285

Maillard, L., Boucharel, J., & Renault, L. (2022). Direct and rectified effects of tropical instability waves on the eastern tropical Pacific mean state in a regional ocean model. *Journal of Physical Oceanography*, *52*(8), 1817–1834. https://doi.org/10.1175/JPO-D-21-0300.1

Mantua, N. J., Hare, S. R., Zhang, Y., Wallace, J. M., & Francis, R. C. (1997). A Pacific interdecadal climate oscillation with impacts on salmon production. *Bulletin of the American Meteorological Society*, *78*(6), 1069–1080. https://doi.org/10.1175/1520-0477(1997)078<1069:APICOW>2.0.CO;2

Masina, S., Philander, S. G. H., & Bush, A. B. G. (1999). An analysis of tropical instability waves in a numerical model of the Pacific Ocean: 2. Generation and energetics of the waves. *Journal of Geophysical Research*, *104*(C12), 29637–29661. https://doi.org/10.1029/1999JC900226

McPhaden, M. J., Ando, K., Bourlès, B., Freitag, H. P., Lumpkin, R., Masumoto, Y., et al. (2010). The Global Tropical Moored Buoy Array. *Proceedings of OceanObs*, *9*, 668–682. https://doi.org/10.5270/OceanObs09.cwp.61

McPhaden, M. J., Connell, K. J., Foltz, G. R., Perez, R. C., & Grissom, K. (2023). Tropical ocean observations for weather and climate: A decadal overview of the Global Tropical Moored Buoy Array. *Oceanography*, *36*(2–3), 32–43. https://doi.org/10.5670/oceanog.2023.211

McPhaden, M. J., Lee, T., & McClurg, D. (2011). El Niño and its relationship to changing background conditions in the tropical Pacific Ocean. *Geophysical Research Letters*, *38*(15), L15709. https://doi.org/10.1029/2011GL048275

McPhaden, M. J., Zebiak, S. E., & Glantz, M. H. (2006). ENSO as an integrating concept in Earth science. *Science*, *314*(5806), 1740–1745. https://doi.org/10.1126/science.1132588

McPhaden, M. J., & Zhang, D. (2002). Slowdown of the meridional overturning circulation in the upper Pacific Ocean. *Nature*, *415*(6872), 603–608. https://doi.org/10.1038/415603a

McPhaden, M. J., & Zhang, D. (2004). Pacific Ocean circulation rebounds. *Geophysical Research Letters*, *31*(18), L18301. https://doi.org/10.1029/2004GL020727

Meehl, G. A., Hu, A., Arblaster, J. M., Fasullo, J., & Trenberth, K. E. (2013). Externally forced and internally generated decadal climate variability associated with the Interdecadal Pacific Oscillation. *Journal of Climate*, *26*(18), 7298–7310. https://doi.org/10.1175/JCLI-D-12-00548.1

Meinen, C. S., McPhaden, M. J., & Johnson, G. C. (2001). Vertical velocities and transports in the equatorial Pacific during 1993-99. *Journal of Physical Oceanography*, *31*(11), 3230–3248. https://doi.org/10.1175/1520-0485(2001)031<3230:VVATIT>2.0.CO;2

Moum, J. N., Hughes, K. G., Shroyer, E. L., Smyth, W. D., Cherian, D., Warner, S. J., et al. (2022). Deep cycle turbulence in Atlantic and Pacific cold tongues. *Geophysical Research Letters*, *49*(8), e2021GL097345. https://doi.org/10.1029/2021GL097345

Newman, M., Alexander, M. A., Ault, T. R., Cobb, K. M., Deser, C., Di Lorenzo, E., et al. (2016). The Pacific decadal oscillation, revisited. *Journal of Climate*, *29*(12), 4399–4427. https://doi.org/10.1175/JCLI-D-15-0508.1

Peng, Q., Xie, S.-P., Wang, D., Huang, R. X., Chen, G., Shu, Y. A., et al. (2022). Surface warming-induced global acceleration of upper-ocean currents. *Science Advances*, *8*(eabj8394). https://doi.org/10.1126/sciadv.abj8394

Perez, R. C., Cronin, M. F., & Kessler, W. S. (2010). Tropical cells and a secondary circulation near the northern front of the equatorial Pacific cold tongue. *Journal of Physical Oceanography*, *40*(9), 2091–2106. https://doi.org/10.1175/2010JPO4366.1

Perez, R. C., Foltz, G. R., Lumpkin, R., & Schmid, C. (2019). Direct measurements of upper ocean horizontal and vertical shear in the tropical North Atlantic at 4°N, 23°W. *Journal of Geophysical Research: Oceans*, *124*(6), 4133–4151. https://doi.org/10.1029/2019JC015064

Perez, R. C., Hormann, V., Lumpkin, R., Brandt, P., Johns, W. E., Hernandez, F., et al. (2014). Mean meridional currents in the central and eastern equatorial Atlantic. *Climate Dynamics*, *43*(11), 2943–2962. https://doi.org/10.1007/s00382-013-1968-5

Power, S., Casey, T., Folland, C., Colman, A., & Mehta, V. (1999). Inter-decadal modulation of the impact of ENSO on Australia. *Climate Dynamics*, *15*(5), 319–324. https://doi.org/10.1007/s003820050284

Power, S., Lengaigne, M., Capotondi, A., Khodri, M., Vialard, J., Jebri, B., et al. (2021). Decadal climate variability in the tropical Pacific: Characteristics, causes, predictability and prospects. *Science*, *374*(6563), eaay9165. https://doi.org/10.1126/science.aay9165

Schott, F. A., & McCreary Jr., J. P. (2001). The Monsoon circulation of the Indian Ocean. *Progress in Oceanography*, *51*(1), 1–123. https://doi.org/10.1016/S0079-6611(01)00083-0

Schott, F. A., McCreary Jr., J. P., & Johnson, G. C. (2004). Shallow overturning circulations of the tropical-subtropical oceans. Earth's climate: The ocean-atmosphere interaction. *Geophysical Monograph Series*, *147*, 261–304. https://doi.org/10.1029/147GM15

Servain, J., Caniaux, G., Kouadio, Y. K., McPhaden, M. J., & Araujo, M. (2014). Recent climatic trends in the tropical Atlantic. *Climate Dynamics*, *43*(11), 3071–3089. https://doi.org/10.1007/s00382-014-2168-7

Storto, A., & Yang, C. (2024). Acceleration of the ocean warming from 1961 to 2022 unveiled by large-ensemble reanalyses. *Nature Communications*, *15*, 545. https://doi.org/10.1038/s41467-024-44749-7

Suarez, M. J., & Schopf, P. S. (1988). A delayed action oscillator for ENSO. *Journal of the Atmospheric Sciences*, *45*(21), 3283–3287. https://doi.org/10.1175/1520-0469(1988)045<3283:ADAOFE>2.0.CO;2

Timmermann, A., McGregor, S., & Jin, F.-F. (2010). Wind effects on past and future regional sea level trends in the southern Indo-Pacific. *Journal of Climate*, *23*(16), 4429–4437. https://doi.org/10.1175/2010JCLI3519.1

Trenberth, K. E., Fasullo, J. T., & Balmaseda, M. A. (2014). Earth's energy imbalance. *Journal of Climate*, *27*(9), 3129–3144. https://doi.org/10.1175/JCLI-D-13-00294.1

Tuchen, F. P., Brandt, P., Lübbecke, J. F., & Hummels, R. (2022). Transports and pathways of the tropical AMOC return flow from Argo data and shipboard velocity measurements. *Journal of Geophysical Research: Oceans*, *127*(2), e2021JC018115. https://doi.org/10.1029/2021JC018115

Tuchen, F. P., Lübbecke, J. F., Brandt, P., & Fu, Y. (2020). Observed transport variability of the Atlantic Subtropical Cells and their connection to tropical sea surface temperature variability. *Journal of Geophysical Research: Oceans*, *125*(12), e2020JC016592. https://doi.org/10.1029/2020JC016592

Tuchen, F. P., Lübbecke, J. F., Schmidtko, S., Hummels, R., & Böning, C. W. (2019). The Atlantic Subtropical Cells inferred from observations. *Journal of Geophysical Research: Oceans*, *124*(11), 7591–7605. https://doi.org/10.1029/2019JC015396

Tuchen, F. P., Perez, R. C., Foltz, G. R., Brandt, P., & Lumpkin, R. (2022). Multidecadal intensification of Atlantic tropical instability waves. *Geophysical Research Letters*, *49*(22), e2022GL101073. https://doi.org/10.1029/2022GL101073

Tuchen, F. P., Perez, R. C., Foltz, G. R., Brandt, P., Subramaniam, A., Lee, S.-K., et al. (2024). Modulation of equatorial currents and tropical instability waves during the 2021 Atlantic Niño. *Journal of Geophysical Research: Oceans*, *129*(1), e2023JC020431. https://doi.org/10.1029/2023JC020431

von Schuckmann, K., Brandt, P., & Eden, C. (2008). Generation of tropical instability waves in the Atlantic Ocean. *Journal of Geophysical Research*, *113*(C8), C08034. https://doi.org/10.1029/2007JC004712

von Schuckmann, K., Cheng, L., Palmer, M. D., Hansen, J., Tassone, C., Aich, V., et al. (2020). Heat stored in the Earth system: Where does the energy go? *Earth System Science Data*, *12*(3), 2013–2041. https://doi.org/10.5194/essd-12-2013-2020

Wang, L.-C., Dao, T. L., & Yu, J.-Y. (2022). Continued weakening of the equatorial Pacific upwelling annual cycle in CMIP5 future projections. *Scientific Reports*, *12*(1), 15595. https://doi.org/10.1038/s41598-022-19874-2

Wang, M., Xie, S.-P., Sasaki, H., Nonaka, M., & Du, Y. (2024). Intensification of Pacific tropical instability waves over the recent three decades. *Nature Climate Change*, *14*(2), 163–170. https://doi.org/10.1038/s41558-023-01915-x

Wang, W., & McPhaden, M. J. (1999). The surface-layer heat balance in the equatorial Pacific Ocean. Part I: Mean seasonal cycle. *Journal of Physical Oceanography*, *29*(8), 1812–1831. https://doi.org/10.1175/1520-0485(1999)029<1812:TSLHBI>2.0.CO;2

Wang, W., & McPhaden, M. J. (2001). Surface layer temperature balance in the equatorial Pacific during the 1997-98 El Niño and 1998-99 La Niña. *Journal of Climate*, *14*(16), 3393–3407. https://doi.org/10.1175/1520-0442(2001)014<3393:SLTBIT>2.0.CO;2

Wills, R. C. J., Dong, Y., Proistosecu, C., Armour, K. C., & Battisti, D. S. (2022). Systematic climate model biases in the large-scale patterns of recent sea-surface temperature and sea-level pressure change. *Geophysical Research Letters*, *49*(17), e2022GL100011. https://doi.org/10.1029/2022GL100011

Xue, A., Jin, F.-F., Zhang, W., Boucharel, J., Zhao, S., & Yuan, X. (2020). Delineating the seasonally modulated nonlinear feedback onto ENSO from tropical instability waves. *Geophysical Research Letters*, *47*(7), e2019GL085863. https://doi.org/10.1029/2019GL085863

Xue, A., Zhang, W., Boucharel, J., & Jin, F.-F. (2021). Anomalous tropical instability wave activity hindered the development of the 2016/17 La Niña. *Journal of Climate*, *34*(13), 5583–5600. https://doi.org/10.1175/JCLI-D-20-0399.1

Yang, C., Giese, B. S., & Wu, L. (2014). Ocean dynamics and tropical Pacific climate change in Ocean reanalyses and coupled climate models. *Journal of Geophysical Research: Oceans*, *119*(10), 7066–7077. https://doi.org/10.1002/2014JC009979

Yu, X., & McPhaden, M. J. (1999a). Seasonal variability in the equatorial Pacific. *Journal of Physical Oceanography*, *29*(5), 925–947. https://doi.org/10.1175/1520-0485(1999)029<0925:SVITEP>2.0.CO;2

Yu, X., & McPhaden, M. J. (1999b). Dynamical analysis of seasonal and interannual variability in the equatorial Pacific. *Journal of Physical Oceanography*, *29*(9), 2350–2369. https://doi.org/10.1175/1520-0485(1999)029<2350:DAOSAI>2.0.CO;2

Zhang, Y., Wallace, J. M., & Battisti, D. S. (1997). ENSO-like interdecadal variability: 1900-93. *Journal of Climate*, *10*(5), 1004–1020. https://doi.org/10.1175/1520-0442(1997)010<1004:ELIV>2.0.CO;2